

The influence of spatial configuration in collective transitions: the importance of being sorted

Daniel Galvis

*Centre for Systems Modelling and Quantitative Biomedicine, University of Birmingham, UK and
Institute of Metabolism and Systems Research (IMSR), University of Birmingham, UK*

David J. Hodson

*Institute of Metabolism and Systems Research (IMSR), University of Birmingham, UK
Centre of Membrane Proteins and Receptors (COMPARE), University of Birmingham, Birmingham, UK
Centre for Endocrinology, Diabetes and Metabolism,
Birmingham Health Partners, Birmingham, UK and
Oxford Centre for Diabetes, Endocrinology and Metabolism,
Radcliffe Department of Medicine, University of Oxford, Oxford, OX3 7LE, UK*

Kyle C. A. Wedgwood

*Living Systems Institute, University of Exeter, UK
EPSRC Hub for Quantitative Modelling in Healthcare, University of Exeter, UK and
College of Engineering, Mathematics and Physical Sciences, University of Exeter, UK*

(Dated: January 20, 2022)

We studied the effects of spatial configuration on collective dynamics in a nearest-neighbour and diffusively coupled lattice of heterogeneous nodes. The networks contained nodes from two populations, which differed in their intrinsic excitability. Initially, these populations were uniformly and randomly distributed throughout the lattice. We then developed an iterative algorithm for perturbing the arrangement of the network such that nodes from the same population were increasingly likely to be adjacent to one another. We found that the global input strength, or *network drive*, necessary to transition the network from a state of quiescence to a state of synchronised and oscillatory activity was decreased as *network sortedness* was increased. Moreover, for weak coupling, we found that regimes of partial synchronisation exist (i.e. 2:1 resonance in the activity of the two populations), which were dependent both on network drive (sometimes in a non-monotonic fashion) and network sortedness.

Keywords: Excitable systems, collective dynamics, beta cell, sortedness

I. INTRODUCTION

Many nonlinear systems exhibit *excitable* behaviour, whereby they exhibit large-amplitude oscillations in response to small-amplitude, transient perturbations. Such excitable dynamics are observed in semiconductor lasers [1, 2], social media networks [3], epidemiology [4], and wildfires [5]. One prominent example is electrically excitable cells, such as neurons [6–8], cardiac cells [9, 10], pituitary cells [11, 12] and pancreatic beta cells [13, 14]. When excitable units are combined into networks, they can generate complex rhythms [15–17]. Interestingly, such networks may also generate dynamics that occur over low-dimensional manifolds of the full system [18–21]. For example, neurons in the

pre-Bötzinger complex fire synchronously to induce the inspiratory and expiratory phases during breathing [22, 23].

Heterogeneity is ubiquitous in natural systems. Whilst often portrayed as an undesirable attribute, it can play an important role in governing network dynamics [24–26]. For example, neurons may coarsely be stratified into excitatory and inhibitory groups, with the former promoting firing behaviour in other neurons and the latter suppressing it. When coupled, these neuronal subtypes give rise to a variety of behaviours, including synchronisation, and enable the network to respond differentially to incoming inputs [27–29]. The classification of neuronal subtypes is becoming ever finer [30, 31] and it remains an open question as to how this heterogeneity governs overall brain dynamics. Even when networks comprise only a single unit type, heterogeneity may still impact the global dynamics. For example, if the natural frequencies of nodes in a coupled oscillator network are too far apart, the network will be unable to synchronise and will instead display more complex rhythms [32].

Here, we explore transitions to synchrony in a locally-coupled network of heterogeneous, excitable nodes. As a motivating example, we consider networks of pancreatic beta cells. Individually, these cells exhibit excitable dynamics akin to the Hodgkin–Huxley model of nerve cells [33]. Cells remain at rest until they receive a significantly large electrical impulse or the extracellular concentration of glucose surpasses a threshold value [34, 35]. Under sustained suprathreshold stimulation, cells exhibit repetitive bursting-type dynamics comprising epochs of firing activity, followed by periods of rest [36]. Beta cells are arranged into diffusively, and locally-coupled networks via channels known as gap junctions [37, 38]. These networks exhibit synchronous bursting activity when exposed to sufficiently high levels of glucose [39]. Although exogenous factors, such as incretin [40] and paracrine [41] signalling influence this coordinated beta cell response, the importance of intercellular coupling has been highlighted in several studies that demonstrate that synchronous beta cell rhythms are disrupted when gap junctions are blocked [42, 43].

Based on empirical evidence from rodents, it has generally been assumed that beta cells form a *syncytium*, such that the activity of the network can be described by a single cell [44–46]. Recent studies have challenged this perspective, highlighting that some ‘leader cells’ disproportionately influence the activity of an entire network made up primarily of ‘follower cells’ [47–50]. One hypothesis suggests that islets are composed of a small number ($\sim 10\%$) of highly excitable cells, with the remainder being less excitable [51]. In this study, we explore how the spatial organisation of these two sub-populations affects the propensity of the whole network to oscillate in a synchronous fashion. The remainder of the manuscript is arranged as follows: In Sec. II, we describe the beta cell model, introduce a metric that captures how sorted a network is with respect to its heterogeneity, and present an algorithm that can generate networks with arbitrary sortedness. In Sec. III, we investigate how dynamic transitions to synchronous bursting depends on the degree of sortedness in the network and end in Sec. IV with concluding remarks.

II. METHODS

A. Mathematical model

We consider a network of N diffusively-coupled excitable cells from a model describing electrical activity in pancreatic beta cells in the presence of glucose [52]. These cells exhibit *bursting* dynamics (in voltage v) when the glucose level, $G \in [0, 1]$, is sufficiently high. The system possesses a slow variable, c , representing Ca^{2+} concentration, which oscillates when the cell is active. We arrange $N = 1,018$ nodes on a hexagonal close-packed (hcp) lattice embedded

within a sphere. Each node is connected to its nearest neighbours via gap-junction coupling. The parameter \bar{g}_L sets the excitability of single cells within the network (Fig. S1). We define two sub-populations of nodes distinguished by their excitability. Population 1 is highly excitable ($\bar{g}_L = 60$) and population 2 is less excitable ($\bar{g}_L = 100$). We then consider the range over G where population 1 nodes are intrinsically active, while population 2 cells are intrinsically inactive. A full description of the mathematical model is provided in Sec. S1 A.

B. Measuring sortedness

To track the degree of sortedness in the network, we define a *node sortedness* measure that, for a given node, measures the proportion of neighbours that are of the same population type. For a general network with nodes attributed to $K \in \mathbb{N}$ populations, the node sortedness, A_i , is defined as

$$A_i = \frac{1}{|J_i|} \sum_{j \in J_i} \chi_{ij}, \quad \chi_{ij} = \sum_{k=1}^K \mu_i^{(k)} \mu_j^{(k)}, \quad i = 1, \dots, N, \quad \mu_i^{(k)} = \begin{cases} 1, & i \in P_k \\ 0, & \text{otherwise} \end{cases}, \quad (1)$$

where the *population sets* P_k contain the indices of the nodes within population $k = 1, \dots, K$ and form a partition over the node indices $\{1, 2, \dots, N\}$, J_i is the set of indices of nodes that are adjacent to node i , $\mu_i^{(k)}$ is an indicator function that takes value 1 if i belongs to population k and value 0 otherwise, and χ_{ij} is an indicator function that takes value 1 when node i and j belong to the same population and value 0 otherwise. For each population, the average node sortedness is defined via

$$\bar{A}_k = \frac{1}{|P_k|} \sum_{n \in P_k} A_n, \quad k = 1, 2, \dots, K. \quad (2)$$

Finally, the *network sortedness* is defined as

$$\mathcal{A} = \frac{1}{K-1} \left(-1 + \sum_{k=1}^K \bar{A}_k \right). \quad (3)$$

where $\mathcal{A} \in [-1/(K-1), 1]$ and, for the present case with $K = 2$, $\mathcal{A} \in [-1, 1]$. For a network in which populations are assigned to nodes following a uniformly random distribution, $\mathcal{A} \approx 0$ since \bar{A}_k is approximately equal to N_k/N where N_k , $k = 1, 2$ is the number of nodes in population k . and therefore $\sum_k \bar{A}_k \approx 1$. An illustration of the computation of the sortedness metrics (1)-(3) is shown in Fig. S8.

C. Modifying network sortedness

Here, we describe our approach for generating networks with different network sortedness. The algorithm works by exchanging the population type of nodes from different populations randomly to increase (or decrease) \mathcal{A} . The algorithm begins by randomly permuting the order of the N indices. The first N_1 indices of the permuted sequence are attributed to P_1 , with the remaining N_2 indices attributed to P_2 , yielding a distribution of population 1 nodes that is uniformly random in space.

On each iteration, a , of the algorithm, pairs of nodes (from different populations) are sampled without replacement from a joint probability density function (pdf)

$$P(X = i, Y = j) = f(i, j), \quad i \in P_1, j \in P_2, \quad (4)$$

where X and Y are random integer variables indicating the node selected from population 1 and 2, respectively. The population types of these nodes are then exchanged, that is, if $i \in P_1$ and $j \in P_2$, then i is added to P_2 and removed from P_1 and vice versa for j . The network sortedness (3) is then recomputed for the adjusted population sets. If the exchange leads to an increase (decrease) in \mathcal{A} , the exchange is accepted and the algorithm proceeds to iteration $a + 1$. If the exchange does not lead to an increase (decrease) in \mathcal{A} , the exchange is rejected and indices i and j are placed back in P_1 and P_2 , respectively. In this case, a new pair of nodes is drawn from f and the process is repeated until either: a pair whose exchange leads to an increase (decrease) in \mathcal{A} is found and the algorithm proceeds to the next iteration; or it is determined that no such pair exists, at which point the algorithm terminates. An example of one iteration of this algorithm is depicted in Fig. S9. We refer to the algorithm in which swaps are accepted only if they lead to an increase (decrease) in \mathcal{A} as the *forward* (*backward*) algorithm. We define \mathcal{A}_a to be the evaluation of \mathcal{A} of the network after a iterations. Running the algorithm to convergence produces the sets $\mathcal{P}_k = \{P_k^a\}_{a=0}^{a_{\text{final}}}$ containing the population sets after each iteration.

1. Modified sortedness metrics

Although the algorithm yields well-sorted networks with a small number of clusters of nodes from population 1, these clusters preferentially form at the edges of the domain. The average node sortedness, as defined in (2), for population 1 is maximised when a single cluster of population 1 nodes is coupled to the smallest possible number of population 2 nodes. This naturally occurs at the edges of the domain, since any cluster of population 1 nodes in the domain interior must be surrounded by population 2 nodes. We are interested in the dynamics that arise as the small population of highly excitable cells forms clusters within the lattice, hence, we wish to remove this tendency for clusters to form at the domain boundary. To overcome this, we use a modified definition of the node sortedness (1)

$$\tilde{A}_i = \frac{1}{J} \sum_{j \in J_i} \chi_{ij} + \frac{\mu_i^{(2)} (J - |J_i|)}{J}, \quad i = 1, \dots, N, \quad (5)$$

where $J = 12$ is the number of connections that interior lattice nodes possess. For nodes with $|J_i| < J$ (i.e., nodes on the domain boundary) the additional term in (5) compared to (1) incorporates a further $J - |J_i|$ connections to population 2 nodes for the purposes of calculating node sortedness values. This procedure is equivalent to assuming that the lattice defining our domain is embedded within a larger lattice of population 2 nodes. An example of the computation of network sortedness using (5) is shown in Fig. 1. Pseudocode for the network sortedness manipulation algorithm is provided in Sec. S1 C.

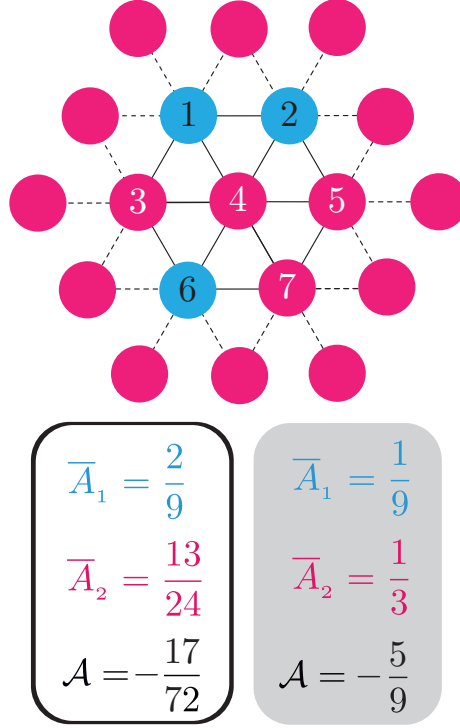


Figure 1. **Example showing the modified sortedness metric.** The network under consideration is the interior portion of the depicted network with population sets $P_1 = \{1, 2, 6\}$ (blue) and $P_2 = \{3, 4, 5, 7\}$ (pink). Using the original node sortedness metric (1), the network sortedness as computed by (3) is $\mathcal{A} = -17/72$. The modified node sortedness (5) assumes that each of the boundary nodes $i \in \{1, 2, 3, 5, 6, 7\}$ has an additional $J - |J_i|$ connections to population 2 nodes, where J_i is the set of nodes to which node i was originally coupled. These additional connections are depicted by the dashed edges emanating from the boundary nodes. In this planar domain example, each of the boundary nodes has $|J_i| = 3$ connections and $J = 6$. Using the modified node sortedness metric, the network sortedness has value $\mathcal{A} = -5/9$.

2. Node selection probabilities

In this section, we formulate the node selection pdf used in the network sortedness adjustment algorithm. We assume that the selection of node from P_1 is independent of the selection of node from P_2 so that (4) becomes

$$f(i, j) = f_{P_1}(i)f_{P_2}(j), \quad i \in P_1, j \in P_2. \quad (6)$$

One choice would set f_1 and f_2 to be uniform over P_1 and P_2 , respectively. Empirical observations of the algorithm outcome in this case demonstrate that clusters of population 1 nodes tend to form at the edge of the domain (not shown). As discussed in Sec. II C 1, we wish to avoid this scenario. The tendency for clusters to form near the edge occurs because of the spherical nature of our lattice domain. In particular, a uniform choice for f_1 and f_2 means that nodes at the centre of the domain are less likely to be selected under a uniformly random sampling of indices than those at the edge because the number of nodes in the network increases superlinearly with respect to the domain radius. Therefore, we derive choices for f_{P_k} that equalise the probability of a node being selected on the basis of its radial coordinate. The heuristic for generating f_{P_1} will be the same as that for generating f_{P_2} up to the population

identity.

Denote the radial distance from the origin of node $i \in \mathbb{N}_N$ by $r_i = (x_i^2 + y_i^2 + z_i^2)^{1/2} \in \mathbb{R}_{\geq 0}$ where $(x_i, y_i, z_i) \in \mathbb{R}^3$ are the Cartesian coordinates of the location of the node. We define a sequences of intervals, $\mathcal{I}_n = [(n-1)\delta r, n\delta r]$, for $n = 1, \dots, 8$ with $\delta r = r_{\max}/8$ where $r_{\max} = \max_i \{r_i\}$ so that each node is assigned to exactly one interval. The set of nodes from P_k belonging to a given interval \mathcal{I}_n is given by $R_{n,P_k} = \{i \in \mathbb{N}_N \mid r_i \in \mathcal{I}_n, i \in P_k\}$. Using these set definitions, the pdf f_{P_k} may be defined as

$$f_{P_k}(i) = \frac{1}{Q|R_{n_i,P_k}|}, \quad i \in \mathbb{N}_N. \quad (7)$$

where R_{n_i,P_k} is such that $r_i \in \mathcal{I}_{n_i}$ and Q is a normalisation factor ensuring that $\sum_{i \in P_k} f_{P_k}(i) = 1$. This choice for f_{P_k} reweights the probability of a given node being selected by a factor proportional to the number of cells from the same population within a spherical annulus with inner and outer radii specified by the boundaries of the intervals \mathcal{I}_n . This reweighting favours selecting nodes closer to the centre of the domain over those more distal.

D. Evaluation of collective dynamics

To characterise the network dynamics, we consider two features based on the Ca^{2+} trajectories across all nodes, namely, the mean number of peaks (\bar{P}) and the time-averaged degree of synchronisation (\bar{R}) calculated as the average magnitude of the Kuramoto order parameter (S13). The mean number of Ca^{2+} peaks across all nodes is proportional to the *network participation*, that is, the fraction of nodes that undergo oscillation. The value of \bar{R} captures the *network coordination*, tracking how closely the phases of the Ca^{2+} trajectories stay to one another across the simulation duration. We additionally define \bar{P}_k and \bar{R}_k where $k \in \{1, 2\}$ to be the mean number of peaks in Ca^{2+} and the time-averaged degree of synchronisation across nodes in population P_k , respectively.

III. RESULTS

A. Simulating dynamics on the set of networks defined by running the swapping algorithm to convergence

We ran the swapping algorithm to convergence (in the forward direction and with 10% of the nodes specified to be from population 1) to produce sets \mathcal{P}_1 and \mathcal{P}_2 . For this run, the network configuration converged after $a_{\text{final}} = 203$ iterations with a corresponding sortedness of the terminal network configuration of $\mathcal{A}_{\text{final}} = 0.69$. We then simulated the dynamical system (S1)-(S11) for 10 equispaced values of $G \in [0.3, 0.55]$, as described in Sec. S1 B for $g_{\text{coup}} \in \{1, 2, 10\}$, and each configuration of populations defined by the population sets contained in \mathcal{P}_1 and \mathcal{P}_2 for $a \in \{1, 4, 7, \dots, a_{\text{final}}\}$. We ran each simulation for $T_{\text{max}} = 360,000$ ms (6 minutes), and discarded the initial 90,000 ms of resulting times series to control for transients. Each network configuration was simulated three times using each of a pre-defined set of initial conditions. Finally, we ran simulations once more using the first of these initial conditions to verify that results were consistent when the simulation duration was increased. We then calculated the features \bar{P} and \bar{R} for each simulation.

To aid in interpreting the results, we define the following sets. Firstly, the parameter domain over which we evaluated the dynamical system was $\mathcal{D} = \{(\mathcal{A}, G) \mid \mathcal{A} \in [0, \mathcal{A}_{\text{final}}], G \in [0.3, 0.55]\}$. Secondly, the level sets $L^+ =$

$\{(\mathcal{A}, G) \mid \bar{P}(\mathcal{A}, G) = 5\}$, $L^* = \{(\mathcal{A}, G) \mid \bar{R}(\mathcal{A}, G) = 0.9\}$, and $L_k^+ = \{(\mathcal{A}, G) \mid \bar{P}_k(\mathcal{A}, G) = 5\}$ (for $k \in 1, 2$) were used to delineate subsets of \mathcal{D} with qualitatively distinct network dynamics, which will be described below.

1. *Increasing \mathcal{A} lowers the drive G required for a transition to globally synchronised bursting when coupling is strong*

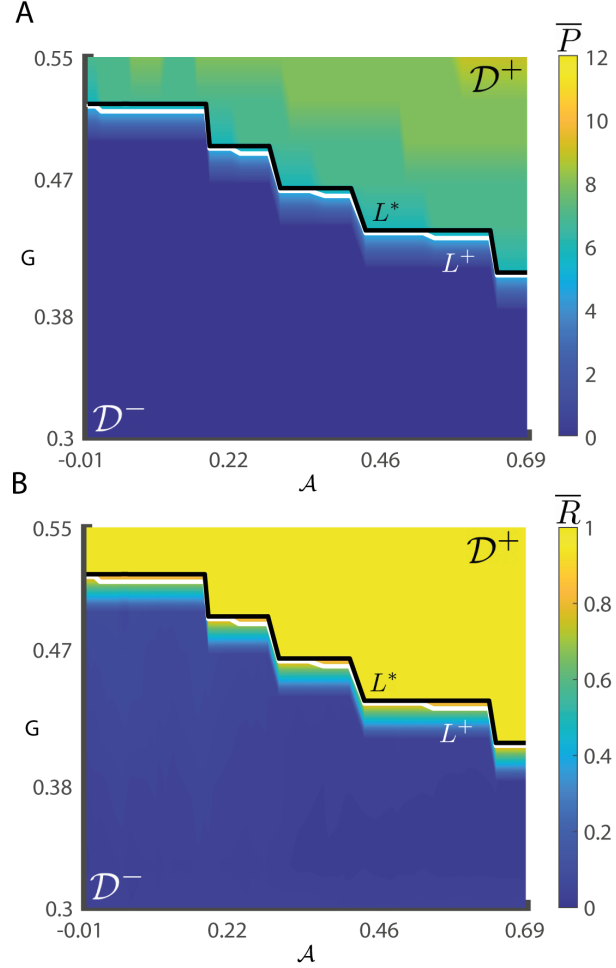


Figure 2. **Network activity with respect to sortedness and drive for strong coupling.** **A)** Plotting \bar{P} averaged over three sets of initial conditions shows that for increasing \mathcal{A} , lower drive G is required to activate the network. **B)** Plotting \bar{R} averaged over three sets of initial conditions shows that for increasing \mathcal{A} , lower drive G is required to synchronise the network.

We first sought to establish whether there is a relationship between \mathcal{A} and the level of drive G required to activate the network. Shown in Fig. S10 is an example in which the transition from global quiescence to global activation is dependent on both G and \mathcal{A} for the strongly coupled ($g_{coup} = 10$) case and where population 1 nodes comprise 10% of the network. The mean of the Ca^{2+} trajectories for population 1 and 2 across the network are plotted for several values of \mathcal{A} and G , which shows that as \mathcal{A} increases, the required drive G to activate the network decreases. To examine trends across a range of network configurations, we plot the features \bar{P} (Fig. 2A, Fig. S11A), and \bar{R} (Fig. 2B, Fig. S11B) as a function of both G and \mathcal{A} . Each point depicts a value $S(\mathcal{A}, G)$, where $S \in \{\bar{P}, \bar{R}\}$, taken to be the median feature across the three simulations (which differ only in their initial condition). For strong coupling,

we found that \mathcal{D} can be separated into a quiescent regime (\mathcal{D}^-) and an oscillatory one (\mathcal{D}^+). The level set curve L^+ separating these regimes can be parameterised as a non-increasing function of \mathcal{A} (i.e., $G = L^+(\mathcal{A})$), supporting the hypothesis that increasing \mathcal{A} decreases the drive required for network activation (Fig. 2A, B white curve). Similarly, the level set L^* can be parameterised as a non-increasing function of \mathcal{A} that also separates the domains \mathcal{D}^- and \mathcal{D}^+ (Fig. 2A, B black curve).

To investigate the robustness of the above relationships, we plotted \bar{P} and \bar{R} resulting from each of the three initial conditions (Fig. S12). We defined curves L^+ (Fig. S12, white curves) and L^* (Fig. S12, black curves), in the same manner as described above. These curves are not identical across the choices of initial condition, and both curves are non-monotonic for the third initial condition, suggesting that multi-stability exists for some $(\mathcal{A}, G) \in \mathcal{D}$, at least near the transition between regimes \mathcal{D}^- and \mathcal{D}^+ .

2. *A domain with intra-population synchronicity and inter-population resonance exists when coupling is lowered to an intermediate strength*

When $g_{coup} = 2$ (intermediate strength coupling), the threshold for activation of the network was lower than in the case of strong coupling, owing to the reduction of the suppressing effect of the less excitable population 2 nodes on the more excitable population 1 nodes. As in Sec. III A 1, we plot the features \bar{P} (Fig. 3A, Fig. S13A) and \bar{R} (Fig. 3B, Fig. S13B) within the parameter domain \mathcal{D} , taking the median across three initial conditions. We observed that the domain can be separated into three regimes with qualitatively distinct dynamics. The first two regimes, \mathcal{D}^- and \mathcal{D}^+ , contain dynamics where the majority of nodes are quiescent or active (Fig. 3A) and synchronised (Fig. 3B), respectively. Within the third regime, denoted \mathcal{D}^* , we found high intra-population synchronisation, with population 2 nodes oscillating (w.r.t. Ca^{2+}) at a frequency approximately half that of the population 1 nodes on average (Fig. S13C, D triangle). i.e., this regime produces inter-population resonance at a 2:1 ratio. Moreover, between the regimes \mathcal{D}^* and \mathcal{D}^+ , we found a sliver of the domain with lowered synchronisation (Fig. S13 star), where the population 2 oscillation frequency approaches that of population 1. For low values of \mathcal{A} , the curves L_k^+ nearly overlap one another and separate the regimes \mathcal{D}^- and \mathcal{D}^+ , however, for larger values of \mathcal{A} , these curves diverge and bound the \mathcal{D}^* regime. Due to the large fraction of nodes being contained in population population 2, we find that the curve L^+ , defined as in Sec. III A 1, approximately overlaps L_2^+ .

The curve L_1^+ marks the transition from quiescence to activity, which may or may not be synchronised, and is non-monotonic. Despite this non-monotonicity, there still exists an overall trend linking increases in \mathcal{A} and the required drive to induce activity, G . In particular, for larger values of \mathcal{A} , where increasing G results in a transition to \mathcal{D}^* , the required drive to pass through L_1^+ is lowest. Moreover, when \mathcal{A} is near \mathcal{A}_0 , i.e., at early iterations of the algorithm, the required drive to pass through L_1^+ is highest (Fig. 3A, B).

When redefining the curves L_k^+ for $k \in \{1, 2\}$ and L^+ for individual sets of initial conditions, we again found that they were not identical, implying the presence multi-stability near the transitions between regimes. In addition, we also found cases of multi-stability within the regime \mathcal{D}^+ (Fig. S14G, H). For example, Fig. S14 shows the plots of \bar{P} (Fig. S14A, C, E) and \bar{R} (Fig. S14B, D, F) resulting from each initial condition separately. For some points (\mathcal{A}, G) , we observed lower synchronisation (\bar{R}) for some initial conditions (Fig. S14 square) relative to the others (Fig. S14 circle). These points of lowered synchrony persisted when T_{max} was increased suggesting that this activity was not

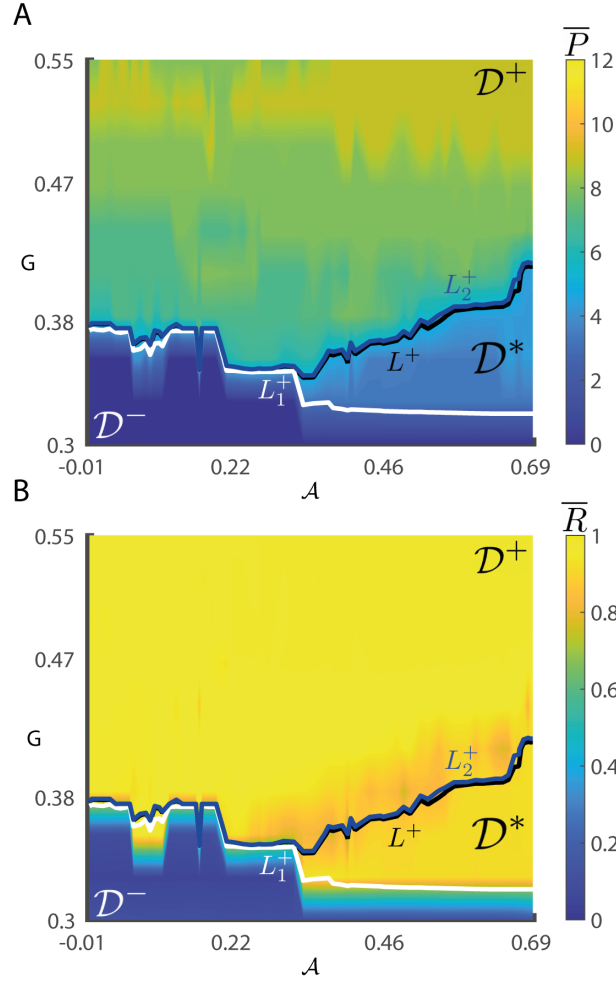


Figure 3. **Network activity with respect to sortedness and drive for middle-strength coupling.** **A)** Plotting \overline{P} averaged over three sets of initial conditions shows a third regime \mathcal{D}^* bounded by L_1^+ and L_2^+ . **B)** Plotting \overline{R} averaged over three sets of initial conditions shows that for increasing \mathcal{A} , lower drive G is required to synchronise the network.

due extended transient behaviour (not shown).

3. When coupling strength is low, only population 1 activation depends on sortedness

When $g_{coup} = 1$ (low coupling strength), we observed a greater variety of parameter regimes supporting distinct dynamics (Fig. 4, Fig. S15) than in either the intermediate strength or strong coupling cases. For this coupling strength, there is no regime in which the network is active and synchronised (i.e., regime \mathcal{D}^+ does not exist). The region \mathcal{D}^- , in which the majority of nodes are inactive, exists for low values of \mathcal{A} and G , and is bounded above by the curve L_1^+ .

We next identified the regime \mathcal{D}_1^+ in which only nodes in P_1 are active while those in P_2 remain silent (Fig. S15, circle). In this regime, population 1 nodes are active but only weakly coordinated while population 2 nodes are mostly inactive (Fig. S15D). This results in a weak global signal (low amplitude oscillations of the average Ca^{2+} signal) (Fig. S15C). This regime can be bounded below by L_1^+ and above by L_2^+ and also by L^+ (not shown). A region,

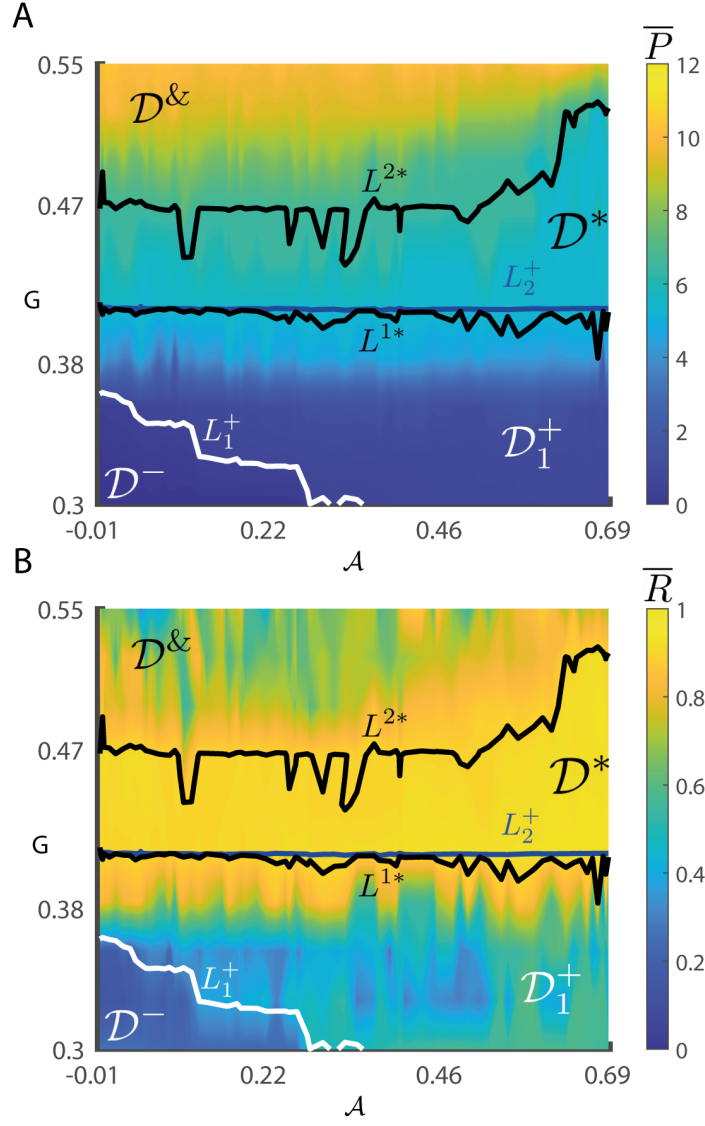


Figure 4. **Network activity with respect to sortedness and drive for weak coupling.** **A)** Plotting \bar{P} averaged over three sets of initial conditions shows that activation of population 1, but not population 2, is dependent on sortedness. **B)** Plotting \bar{R} averaged over three sets of initial conditions shows that synchronisation is non-monotonic with respect to G , peaking within a 2 : 1 resonance regime \mathcal{D}^* .

denoted \mathcal{D}^* , also exists with similar dynamics to the one defined for $g_{coup} = 2$. Within this regime, the overall network synchronisation is high (Fig. 4B), however, population 2 nodes exhibit oscillatory Ca^{2+} behaviour with approximately half the frequency of that of the population 1 nodes (Fig. S15C, D triangle).

A final region, $\mathcal{D}^\&$, exists for high values of G , where network synchronisation decreases (Fig. 4B) whilst the average number of peaks continues to increase (Fig. 4A). The level set L^* defines two separate curves, labelled L_1^* and L_2^* , due to the non-monotonicity of the synchronisation index with respect to G . The curve L_2^* bounds \mathcal{D}^* from above and separates it from $\mathcal{D}^\&$, whilst L_1^* is a lower bound for \mathcal{D}^* and separates it from \mathcal{D}_1^+ . Fig. S15C (star) shows the irregular global signal caused by weak coordination, which is shown in Fig. S15D (star). As in the case for $g_{coup} = 2$, the curve L_1^+ marks the transition from quiescence to activity, however, in this case only population 1 nodes become

active. This curve is non-monotonic, however, the overall trend once again links increases in \mathcal{A} with a lower required drive to induce activity. On the other hand, the curve L_2^+ does not appear to be dependent on \mathcal{A} . Additionally, we found that the curve $G = L^{2*}(\mathcal{A})$, defined by the set L^{2*} , shows an increasing trend, which suggests that the range of G for which maximal synchronisation occurs increases with \mathcal{A} .

IV. DISCUSSION

In this manuscript, we demonstrated how transitions to globally-coordinated activity are dependent on the degree of sortedness in population excitability. We used a prototypical model of a pancreatic beta cell where a small population was highly excitable, whilst a larger population was less excitable. As the global drive to the network was increased, activity across the network transitioned from a globally inactive state to one in which subsets of nodes became active and synchronised their activity. By perturbing the spatial distribution of the highly excitable population, we showed that the drive strength at which such transitions occur is dependent on the sortedness of the network. These results have specific implications for insulin secretion in the pancreatic islets of Langerhans, and more general implications regarding transitions to synchrony and other forms of collective dynamics in networks of coupled excitable units.

To perform our study, we developed Algorithm 1, which perturbs the sortedness of the network in a directed manner. Whilst our algorithm is tailored towards spherical geometries and local, diffusive coupling, it can be adapted to other geometries and coupling types, since the neighbourhoods can be succinctly encoded in the adjacency matrix. In addition, although our study focused on conditions in which there are only two different populations, Sec. II discusses how our metrics can be extended to networks with more population types. Given the growing interest in studying heterogeneous populations in complex networks, we hope that our algorithms will prove useful to other researchers in the future.

V. ACKNOWLEDGEMENTS

DG acknowledges funding from the University of Birmingham Dynamic Investment Fund and the EPSRC Centre grant EP/N014391/2. DJH acknowledges funding from the MRC Projects MR/N00275X/1 and MR/S025618/1 the and Diabetes UK Project Grants 17/0005681. This project has also received funding from the European Research Council (ERC) under the European Union's Horizon 2020 research and innovation programme (Starting Grant 715884 to DJH). KCAW acknowledges funding from the MRC Fellowship MR/P01478X/1 and the Hub for Quantitative Modelling in Healthcare EP/T017856/1.

-
- [1] S. Terrien, V. A. Pammi, N. G. R. Broderick, R. Braive, G. Beaudoin, I. Sagnes, B. Krauskopf, and S. Barbay, Physical Review Research **2**, 10.1103/physrevresearch.2.023012 (2020), arXiv:1907.11143.
 - [2] S. Terrien, V. A. Pammi, B. Krauskopf, N. G. Broderick, and S. Barbay, Physical Review E **103**, 10.1103/PhysRevE.103.012210 (2021), arXiv:2006.11010.
 - [3] J. Mathiesen, L. Angheluta, P. T. Ahlgren, and M. H. Jensen, Proceedings of the National Academy of Sciences of the United States of America **110**, 17259 (2013).

- [4] F. Vannucchi and S. Boccaletti, *Mathematical Biosciences and Engineering* **1**, 49 (2004).
- [5] C. Punckt, P. S. Bodega, P. Kaira, and H. H. Rotermund, *Journal of Chemical Education* **92**, 1330 (2015).
- [6] E. M. Izhikevich, *International Journal of Bifurcation and Chaos* **10**, 1171 (2000).
- [7] P. De Maesschalck and M. Wechselberger, *Journal of Mathematical Neuroscience* **5**, 10.1186/s13408-015-0029-2 (2015).
- [8] K. C. Wedgwood, P. Słowiński, J. Manson, K. Tsaneva-Atanasova, and B. Krauskopf, *Journal of the Royal Society Interface* **18**, 10.1098/rsif.2021.0029 (2021).
- [9] R. Majumder, I. Feola, A. S. Teplenin, A. A. de Vries, A. V. Panfilov, and D. A. Pijnappels, *eLife* **7**, 1 (2018).
- [10] R. Barrio, S. Coombes, M. Desroches, F. Fenton, S. Luther, and E. Pueyo, *Communications in Nonlinear Science and Numerical Simulation* **86**, 10.1016/j.cnsns.2020.105275 (2020).
- [11] C. Sanchez-Cardenas, P. Fontanaud, Z. He, C. Lafont, A. C. Meunier, M. Schaeffer, D. Carmignac, F. Molino, N. Coutry, X. Bonnefont, L. A. Gouty-Colomer, E. Gavois, D. J. Hodson, P. Le Tissier, I. C. Robinson, and P. Mollard, *Proceedings of the National Academy of Sciences of the United States of America* **107**, 21878 (2010).
- [12] D. J. Hodson, M. Schaeffer, N. Romanò, P. Fontanaud, C. Lafont, J. Birkenstock, F. Molino, H. Christian, J. Lockey, D. Carmignac, M. Fernandez-Fuente, P. Le Tissier, and P. Mollard, *Nature Communications* **3**, 10.1038/ncomms1612 (2012).
- [13] R. Bertram, L. S. Satin, M. G. Pedersen, D. S. Luciani, and A. Sherman, *Biophysical Journal* **92**, 1544 (2007).
- [14] J. P. McKenna, J. Ha, M. J. Merrins, L. S. Satin, A. Sherman, and R. Bertram, *Biophysical Journal* **110**, 733 (2016).
- [15] P. Bittihn, S. Berg, U. Parlitz, and S. Luther, *Chaos* **27**, 10.1063/1.4999604 (2017).
- [16] M. Hörning, F. Blanchard, A. Isomura, and K. Yoshikawa, *Scientific Reports* **7**, 1 (2017).
- [17] C. Fretter, A. Lesne, C. C. Hilgetag, and M. T. Hütt, *Scientific Reports* **7**, 1 (2017), arXiv:1403.6174.
- [18] P. Ashwin and J. W. Swift, *Journal of Nonlinear Science* **2**, 69 (1992).
- [19] S. Watanabe and S. H. Strogatz, *Physical Review Letters* **70**, 2391 (1993).
- [20] E. Ott and T. M. Antonsen, *Chaos* **19**, 10.1063/1.3136851 (2009), arXiv:0902.2773.
- [21] C. Bick, M. Goodfellow, C. R. Laing, and E. A. Martens, *Journal of Mathematical Neuroscience* **10**, 10.1186/s13408-020-00086-9 (2020), arXiv:1902.05307.
- [22] S. Wittmeier, G. Song, J. Duffin, and C. S. Poon, *Proceedings of the National Academy of Sciences of the United States of America* **105**, 18000 (2008).
- [23] C. Gaiteri and J. E. Rubin, *Frontiers in Computational Neuroscience* **5**, 10.3389/fncom.2011.00010 (2011).
- [24] K. Manchanda, A. Bose, and R. Ramaswamy, *Physica A: Statistical Mechanics and its Applications* **487**, 111 (2017).
- [25] M. d. M. Delgado, M. Miranda, S. J. Alvarez, E. Gurarie, W. F. Fagan, V. Penteriani, A. di Virgilio, and J. M. Morales, *Philosophical Transactions of the Royal Society B: Biological Sciences* **373**, 10.1098/rstb.2017.0008 (2018).
- [26] D. Lambert and F. Vanni, *Chaos, Solitons and Fractals* **108**, 94 (2018).
- [27] C. Börgers and N. Kopell, *Neural Computation* **15**, 509 (2003).
- [28] C. Börgers, S. Epstein, and N. J. Kopell, *Proceedings of the National Academy of Sciences of the United States of America* **102**, 7002 (2005).
- [29] N. Kopell, M. A. Kramer, P. Malerba, and M. A. Whittington, *Frontiers in Human Neuroscience* **4**, 1 (2010).
- [30] N. W. Gouwens, S. A. Sorensen, J. Berg, C. Lee, T. Jarsky, J. Ting, S. M. Sunkin, D. Feng, C. A. Anastassiou, E. Barkan, K. Bickley, N. Blesie, T. Braun, K. Brouner, A. Budzillo, S. Caldejon, T. Casper, D. Castelli, P. Chong, K. Crichton, C. Cuhaciyan, T. L. Daigle, R. Dalley, N. Dee, T. Desta, S. L. Ding, S. Dingman, A. Doperalski, N. Dotson, T. Egdorf, M. Fisher, R. A. de Frates, E. Garren, M. Garwood, A. Gary, N. Gaudreault, K. Godfrey, M. Gorham, H. Gu, C. Habel, K. Hadley, J. Harrington, J. A. Harris, A. Henry, D. J. Hill, S. Josephsen, S. Kebede, L. Kim, M. Kroll, B. Lee, T. Lemon, K. E. Link, X. Liu, B. Long, R. Mann, M. McGraw, S. Mihalas, A. Mukora, G. J. Murphy, L. Ng, K. Ngo, T. N. Nguyen, P. R. Nicovich, A. Oldre, D. Park, S. Parry, J. Perkins, L. Potekhina, D. Reid, M. Robertson, D. Sandman, M. Schroedter,

- C. Slaughterbeck, G. Soler-Llavina, J. Sulc, A. Szafer, B. Tasic, N. Taskin, C. Teeter, N. Thatra, H. Tung, W. Wakeman, G. Williams, R. Young, Z. Zhou, C. Farrell, H. Peng, M. J. Hawrylycz, E. Lein, L. Ng, A. Arkhipov, A. Bernard, J. W. Phillips, H. Zeng, and C. Koch, *Nature Neuroscience* **22**, 1182 (2019).
- [31] M. Lipovsek, C. Bardy, C. R. Cadwell, K. Hadley, D. Kobak, and S. J. Tripathy, *Journal of Neuroscience* **41**, 937 (2021).
- [32] B. Ottino-Löffler and S. H. Strogatz, *Physical Review E* **93**, 10.1103/PhysRevE.93.062220 (2016), arXiv:1512.02321.
- [33] A. L. Hodgkin and A. F. Huxley, *Journal of Physiology* **117**, 500 (1952).
- [34] Ashcroft Frances M and P. Rorsman, *Progress in Biophysics and Molecular Biology* **54**, 87 (1989).
- [35] M. Braun, R. Ramracheya, M. Bengtsson, Q. Zhang, J. Karanauskaite, C. Partridge, P. R. Johnson, and P. Rorsman, *Diabetes* **57**, 1618 (2008).
- [36] T. A. Kinard, G. De Vries, A. Sherman, and L. S. Satin, *Biophysical Journal* **76**, 1423 (1999).
- [37] P. Rorsman and M. Braun, *Annual Review of Physiology* **75**, 155 (2013).
- [38] R. K. P. Benninger, W. S. Head, M. Zhang, L. S. Satin, and D. W. Piston, *The Journal of Physiology* **589**, 5453 (2011).
- [39] R. Markovič, A. Stožer, M. Gosak, J. Dolenšek, M. Marhl, and M. S. Rupnik, *Scientific reports* **5**, 7845 (2015).
- [40] D. J. Hodson, A. I. Tarasov, S. G. Brias, R. K. Mitchell, N. R. Johnston, S. Haghollahi, M. C. Cane, M. Bugliani, P. Marchetti, D. Bosco, P. R. Johnson, S. J. Hughes, and G. A. Rutter, *Molecular Endocrinology* **28**, 860 (2014).
- [41] A. Caicedo, *Seminars in Cell and Developmental Biology* **24**, 11 (2013), arXiv:NIHMS150003.
- [42] W. S. Head, M. L. Orseth, C. S. Nunemaker, L. S. Satin, D. W. Piston, and R. K. P. Benninger, *Diabetes* **61**, 1700 (2012).
- [43] R. K. P. Benninger and D. W. Piston, *Trends in Endocrinology and Metabolism* **25**, 399 (2014), arXiv:NIHMS150003.
- [44] J. Dolenšek, A. Stožer, M. S. Klemen, E. W. Miller, and M. S. Rupnik, *PLoS ONE* **8**, 1 (2013).
- [45] L. S. Satin, Q. Zhang, and P. Rorsman, *Diabetes* **69**, 830 (2020).
- [46] B. Podobnik, D. Korošak, M. Skelin Klemen, A. Stožer, J. Dolenšek, M. Slak Rupnik, P. C. Ivanov, P. Holme, and M. Jusup, *Biophysical Journal* **118**, 2588 (2020).
- [47] N. R. Johnston, R. K. Mitchell, E. Haythorne, D. Trauner, G. A. Rutter, D. J. Hodson, N. R. Johnston, R. K. Mitchell, E. Haythorne, M. P. Pessoa, F. Semplici, J. Ferrer, L. Piemonti, P. Marchetti, M. Bugliani, D. Bosco, E. Berishvili, and P. Duncanson, *Cell Metabolism* **24**, 389 (2016).
- [48] M. J. Westacott, N. W. Ludin, and R. K. Benninger, *Biophysical Journal* **113**, 1093 (2017).
- [49] V. Salem, L. Silva, K. Suba, E. Georgiadou, S. Neda Mousavy Gharavy, N. Akhtar, A. Martin-alonso, D. Gaboriau, S. Rothery, T. Stylianides, G. Carrat, T. Pullen, S. Singh, D. Hodson, I. Leclerc, A. Shapiro, P. Marchetti, L. Briant, W. Distaso, N. Ninov, and G. Rutter, *Nature Metabolism* **1**, 615 (2019).
- [50] R. K. Benninger and V. Kravets, *Nature Reviews Endocrinology* **0123456789**, 10.1038/s41574-021-00568-0 (2021).
- [51] R. K. Benninger and D. J. Hodson, *Diabetes* **67**, 537 (2018).
- [52] A. Sherman, J. Rinzel, and J. Keizer, *Biophysical Journal* **54**, 411 (1988).
- [53] B. Ermentrout, *Simulating, Analysing and Animating Dynamical Systems: A Guide to XPPAUT for Researchers and Students* (SIAM, 2002).

S1. SUPPLEMENTAL MATERIAL

A. Mathematical model

We consider a network of N diffusively coupled excitable cells, each of which is described by the three variable model

$$C_m \frac{dV_i}{dt} = -I_K(V_i, n_i) - I_{Ca}(V_i, h_i) - I_{K-Ca}(V_i, c_i) - I_L(V_i) - I_{coup,i}, \quad i = 1, \dots, N, \quad (S1)$$

$$\frac{dn_i}{dt} = \frac{n_\infty(V_i) - n_i}{\tau_n(V_i)}, \quad (S2)$$

$$\frac{dc_i}{dt} = -f(\alpha I_{Ca}(V_i, c_i) + k_{Ca} c_i). \quad (S3)$$

This system was adapted from the Sherman–Rinzel–Keizer model, which describes the dynamics of electrical activity in pancreatic beta cells in the presence of glucose [52]. The intrinsic dynamics of the voltage, V given by (S1) are driven by K^+ (I_K), Ca^{2+} (I_{Ca}), and Ca^{2+} -activated K^+ (I_{K-Ca}) ionic currents, with a rate governed by the whole cell capacitance given by C_m . These currents are described via

$$I_K(V, n) = \bar{g}_K n (V - V_K), \quad (S4)$$

$$I_{Ca}(V, h) = \bar{g}_{Ca} m_\infty(V) h_\infty(V) (V - V_{Ca}), \quad (S5)$$

$$I_{K-Ca}(V, c) = \bar{g}_{K-Ca} \frac{c}{K_d + c} (V - V_K), \quad (S6)$$

$$I_L(V) = \bar{g}_L (1 - G) (V - V_K). \quad (S7)$$

In (S4)-(S7), \bar{g}_X denotes the maximal conductance of the channel X where $X \in \{K, Ca, K - Ca, L\}$ where L signifies a leak channel; V_X are the reversal potentials of the respective channels, m and n are the proportion of open activating gates for the Ca^{2+} and K^+ channels, respectively; h is the proportion of open inactivating Ca^{2+} channels; c is the cytosolic concentration of Ca^{2+} ; and G is the extracellular concentration of glucose, which provides a global drive to promote activity and is taken to be homogeneous across the network. The activation of I_{K-Ca} is a function of free intracellular Ca^{2+} concentration and is defined by a Hill-type function with disassociation constant K_d . The current $I_{coup,i}$ captures the influence of the coupling between cells and will be discussed in Sec. S1 B 3.

The dynamics for n and h follow exponential decay to their state values given by

$$x_\infty(V) = \frac{1}{1 + \exp[(V_x - V)/S_x]}, \quad x \in \{h, m, n\}, \quad (S8)$$

at a rate given by the voltage-dependent time constant

$$\tau_n(V) = \frac{\bar{\tau}}{\exp[(V - \bar{V})/\kappa_1] + \exp[-(V - \bar{V})/\kappa_2]}. \quad (S9)$$

In (S8), V_x represents the activation (inactivation) thresholds for m and n (h) and S_x represents the sensitivity of the channels around this point. Finally, (S3) describes the evolution of the concentration of cytosolic Ca^{2+} , which decays and is pumped out of the cell following a combined linear process with rate k_{Ca} and enters the cell via the Ca^{2+} ion channel at a rate given by the scale factor α . The parameter f specifies the fraction of free to bound Ca^{2+} in the cell, where the bound Ca^{2+} plays no role in the relevant dynamics in our model.

The electrical activity of pancreatic beta cells is proportional to the extracellular concentration of glucose. For sufficiently high extracellular glucose, the cells exhibit *bursting* dynamics, in which their voltage periodically switches

Parameter	Value	Parameter	Value	Parameter	Value
C_m (fF)	5310	V_m (mV)	4	S_m (mV)	14
V_n (mV)	-15	S_n (mV)	5.6	κ_1 (mV)	65
κ_2 (mV)	20	$\bar{\tau}$ (ms)	37.5	\bar{V} (mV)	-75
V_h (mV)	-10	S_h (mV)	-10	\bar{g}_K (pS)	2500
\bar{g}_{Ca} (pS)	1400	V_K (mV)	-75	V_{Ca} (mV)	110
K_d (μ M)	100	\bar{g}_{K-Ca} (pS)	30000	f	0.001
k_{Ca} (ms^{-1})	0.03	$\alpha \left(\frac{\mu\text{m}^3 \text{Coul}}{\text{mMol}} \right)$	4.5061×10^{-6}	\bar{g}_{coup} (pS)	{varies}

Table S1. Parameter values of the oscillator model.

between high frequency oscillations and quiescence. The high frequency oscillations in voltage are correlated with the secretion of insulin from these cells, so that these bursting dynamics are tightly coupled to the cells' functional role. To expose the dependence of our system on glucose, we introduced a hyperpolarising leak current given by (S7) that explicitly depends on the glucose concentration G . For an isolated cell (i.e., without coupling) with the parameters specified in Table S1, the system describing each node exhibits steady state behaviour for low G and passes through a bifurcation as $G \in [0, 1]$ is increased, as shown in Fig. S1.

The bursting dynamics in our model are of the *fold-homoclinic* type under the classification specified in [6]. This classification is based on separation of the full system into a fast subsystem (S1)-(S2) and a slow subsystem (S3), treating the slow subsystem variables (in this case, c) as parameters in the fast subsystem. During each bursting cycle, the slow evolution of c pushes the fast subsystem through bifurcations that initiate and terminate oscillatory behaviour. In particular, when c decreases to a small enough value, the fast subsystem passes through a fold bifurcation in which a stable steady state and a saddle steady state collide and annihilate one another. Following this, the system exhibits stable periodic activity, during which c increases according to (S3). When c increases to a sufficiently large value, the fast subsystem passes through a homoclinic bifurcation that destroys the periodic orbit and the system returns to the original stable steady state. Following this, c decreases until it once again reaches the fold point and the cycle repeats.

B. Model simulations

Simulations were conducted using Matlab 2019B. The dynamical systems were solved using ode15s, the relative tolerance set to 10^{-5} , and explicit Jacobians were provided. The code was run on the University of Birmingham BlueBEAR HPC running RedHat 8.3 (x86_64) (see <http://www.birmingham.ac.uk/bear> for more details). Each set of simulations ran over 16 cores using a maximum of 128GB RAM (32GB was sufficient in most cases). All code used in the project is freely available for download from: github.com/dgalvis/network_spatial.

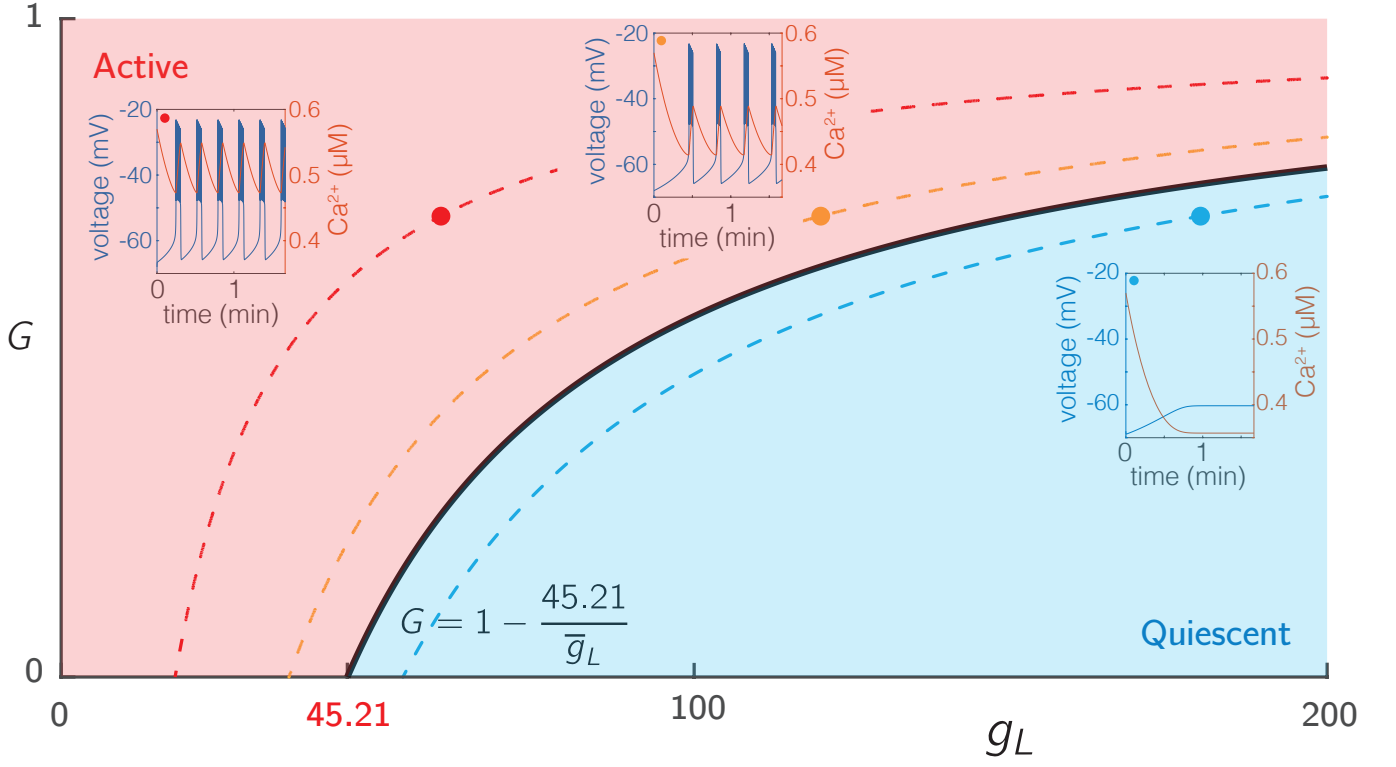


Figure S1. **Excitability of single cells.** The voltage traces from three cells with varying levels of intrinsic excitability (\bar{g}_L), but the same level of drive ($G = 0.7$). The red, blue, and black traces show decreasing levels of excitability with values of $\bar{g}_L = 60, 120$, and 180 , respectively. More excitable cells have a shorter interburst interval. The solid black line represents a Hopf bifurcation as a function of both G and g_L . At the lowest drive ($G = 0$), the Hopf bifurcation occurs for $\bar{g}_L = 45.21$ pS. The dotted lines represent “level sets” of the (\bar{g}_L, G) parameter space, along which the excitability of the single cell is identical. Data for the bifurcation diagram was computed using XPP 8.0 [53].

1. Initial Conditions

Initial conditions $y_i(0) = (V_i(0), n_i(0), c_i(0))$ for node $i = 1, \dots, N$ were sampled independently from the distributions

$$V_i(0) \sim \mathcal{N}(-68, (68/6)^2), \quad n_i(0) = 0, \quad c_i(0) \sim \mathcal{N}(0.57, (0.57/6)^2), \quad (\text{S10})$$

where $\mathcal{N}(\mu, \sigma^2)$ represents a normal distribution with mean μ and variance σ^2 . Throughout, we use $Y(0)$ to denote the set of initial conditions across the whole network, i.e., $Y(0) = (y_1(0), \dots, y_N(0))$.

2. Excitability and drive in the single-cell model

The ionic current I_L (S7) is a hyperpolarising current that can be used to adjust the excitability of each cell and to determine the activation level of the network. In particular, the maximum conductance \bar{g}_L determines the excitability of a cell. As this value increases, the cell becomes less excitable, that is, for a given value of G , cells with higher \bar{g}_L are less likely to burst. This behaviour is summarised in Fig. S1, which shows a two parameter bifurcation diagram

showing the transition from quiescent to bursting behaviour under simultaneous variation of (\bar{g}_L, G) , which occurs via a Hopf bifurcation of the full system (S1)-(S3). For $G = 0$, this Hopf bifurcation occurs at $\bar{g}_L = 45.21$ pS. For non-zero values of G , the bifurcation curve is defined via $(1 - G)\bar{g}_L = 45.21$ pS, as can be seen by examining the form of the (S1) and (S7). Note that when $G = 1$, system (S1)-(S3) matches that of [52]. In the network modelling approach, we use the observations about the link between \bar{g}_L and excitability to partition the network into two sub-populations, one being highly excitable, the other being significantly less excitable.

3. Network structure and coupling

Pancreatic beta cells are arranged into roughly spherical clusters called islets of Langerhans (which also encompass other cell types which are disregarded in our model), which each contain $\sim 1,000$ beta cells. To capture this, we arrange $N = 1,018$ nodes on a hexagonal close packed (hcp) lattice embedded within a sphere. The dominant form of coupling between beta cells in the islets is through gap junctions, which allow small molecules, including charged ions to pass directly from a cell to its adjacent neighbours. Mathematically, this is represented through the inclusion of the diffusive term $I_{coup,i}$ in (S1) that factors in the local nature of coupling

$$I_{coup,i} = \bar{g}_{coup} \sum_{j \in J_i} (V_i - V_j), \quad (\text{S11})$$

where J_i is the set of all cells to which cell i is coupled. Each node is connected to all of its nearest-neighbours so that the number of connections of nodes away from the boundary of the sphere is equal to the coordination number 12 whilst nodes on the boundary have fewer connections.

4. Heterogeneity

We consider networks consisting of two sub-populations of nodes distinguished by their excitability (i.e., by their \bar{g}_L values). Population 1 is highly excitable ($\bar{g}_L = 60$ pS) and population 2 is less excitable ($\bar{g}_L = 100$ pS). We then consider the range over G for which population 1 nodes are intrinsically active (i.e., when $\bar{g}_{coup} = 0$) and population 2 nodes are intrinsically quiescent. We then consider the effects of population size (by varying the proportion of overall network that population 1 nodes account for), the degree of sortedness between the two subpopulations (see Sec. II B), global network drive (G), and global coupling strength on the collective dynamics of the network.

C. Description of the routines used by Algorithm 1

Algorithm 1 Algorithm for producing networks

Inputs:

N : number of nodes in network
 a : number of iterations of swapping algorithm to attempt
 Dir : signed integer determining whether algorithm runs forwards (positive) or backwards (negative)
 ρ : proportion of population 1 nodes

Outputs:

\mathcal{A} : network sortedness value
 P_1 : population 1 set
 P_2 : population 2 set
 n : number of swaps performed

```

1: function GENERATENETWORK( $N, a, Dir, \rho$ )
2:    $(x, y, z), r, K \leftarrow \text{ESTABLISHLATTICE}(N)$ 
3:    $N_1, N_2, P_1, P_2, \mathcal{A} \leftarrow \text{ASSIGNINITIALPOPULATIONS}(N, \rho)$ 
4:    $Term \leftarrow \text{false}$  ▷ Boolean determining whether terminal network state has been reached
5:    $n \leftarrow 0$ 
6:   while ( $n < a$ ) and ( $Term = \text{false}$ ) do
7:      $f, F, Q \leftarrow \text{COMPUTESELECTIONPROBABILITIES}(r[], N_1, N_2, P_1, P_2)$ 
8:      $m \leftarrow 0$ 
9:      $swap \leftarrow \text{true}$  ▷ Boolean determining whether to attempt swaps
10:    while ( $m < N_1 \times N_2$ ) and ( $swap = \text{true}$ ) do
11:       $\tilde{P}_1, \tilde{P}_2, \mathcal{A}_p, k \leftarrow \text{NODESWAP}(f, F, Q, Dir, N_1, N_2, P_1, P_2)$ 
12:      if  $\text{sgn}(\mathcal{A}_p - \mathcal{A}) = \text{sgn}(Dir)$  then
13:         $P_1, P_2 \leftarrow \tilde{P}_1, \tilde{P}_2$ 
14:         $\mathcal{A} \leftarrow \mathcal{A}_p$ 
15:         $n \leftarrow n + 1$ 
16:         $swap \leftarrow \text{false}$ 
17:      else ▷ Reject swap if  $\mathcal{A}$  does not change in the desired direction
18:        for  $l \leftarrow k$  to  $N_1 \times N_2$  do
19:           $F[l] \leftarrow F[l] - f[k]$ 
20:        end for
21:         $Q \leftarrow Q - f[k]$ 
22:         $m \leftarrow m + 1$ 
23:      end if
24:    end while
25:    if  $swap = \text{true}$  then
26:       $Term \leftarrow \text{true}$  ▷ Terminal state has been reached
27:    end if
28:  end while
29:  return  $\mathcal{A}, P_1, P_2, n$ 
30: end function

```

Algorithm 2-Algorithm 7 are used by Algorithm 1 which is described in the main text.

Algorithm 2 returns a set of points in \mathbb{R}^3 corresponding to the centres of spheres within a hexagonal close packed lattice (hcp). The input r_{ball} corresponds to the radius of the spheres within the lattice, which we set to $r_{ball} = 0.5$ so that the distance between any two nearest neighbors is $d_{ball} = 2r_{ball} = 1$. Algorithm 2 produces the hcp lattice using a sequence of scalings and shifts of a square lattice which takes the points $\{(x, y, z) \mid x, y, z \in \{1, \dots, M\}\}$, where M is an integer corresponding to the number of spheres along the length of the lattice. We sought to embed

a larger sphere, S_{net} , of radius R_{net} within the resulting hcp-lattice, and therefore, must choose M such that S_{net} is contained within the lattice. For the square lattice, a natural choice would be $M = 2R_{net}$, so that the length of the lattice equals the diameter of the sphere. However, for the hcp-lattice, the size of the resulting structure is $(M - 1)x_{scale} + d_{ball} = Mx_{scale} = Md_{ball}$ by $(M - 1)y_{scale} + d_{ball} > My_{scale}$ by $(M - 1)z_{scale} + d_{ball} > Mz_{scale}$ (ignoring the shifts). To counteract this, we use:

$$M = \text{ceil} \left(\frac{2R_{net}}{\min([x_{scale}, y_{scale}, z_{scale}])} \right). \quad (\text{S12})$$

We found that this choice of M generated a lattice which could fully embed the sphere, at least for our selection of $R_{net} = 5.55$ (in particular, we increased M and found that the number of nodes within the sphere did not increase).

Algorithm 3 first runs Algorithm 2 to produce an hcp-lattice. It then centres the lattice at the origin (i.e., at $(0, 0, 0)$) and finds all points that are within a sphere of radius R_{net} centred at the origin, which define the nodes in the network. It also returns N , the number of nodes in the spherical hcp-lattice ($N = 1,018$ in this work). Algorithm 4 establishes the Boolean adjacency matrix representing the connections between nodes in the spherical hcp-lattice. A connection exists between two nodes if they are at a distance of d_{ball} from one another. In other words, if two spheres (of radius r_{ball}) centred at the locations assigned to two nodes would be touching, then a connection exists between them. Algorithm 5 determines the population sets P_k for $k \in 1, 2$. It returns the number of nodes N_k in each population, the population membership sets, and the initial network sortedness value A_0 . Algorithm 6 determines the selection probabilities for every pair of nodes ($\{(i, j) \mid i \in P_1, j \in P_2\}$). Algorithm 7 chooses a candidate swap, produces the population sets established by that swap, and calculates \mathcal{A} for the updated population sets.

Algorithm 2 Initialising HCP lattice

Inputs:

R_{net} : radius of the spherical lattice
 r_{ball} : radius of balls around points in the lattice

Outputs:

$(x_1, y_1, z_1), \dots, (x_N, y_N, z_N)$: (x, y, z) coordinates of nodes
 N : number of nodes in hcp-lattice

```

1: function ESTABLISHHCPLATTICE( $R_{net}, r_{ball}$ )
2:    $d_{ball} \leftarrow 2r_{ball}$ 
3:    $x_{scale} \leftarrow d_{ball}$ 
4:    $y_{scale} \leftarrow \sqrt{d_{ball}^2 - r_{ball}^2}$ 
5:    $z_{scale} \leftarrow \sqrt{\frac{2}{3}}d_{ball}$ 
6:    $x_{shift} \leftarrow r_{ball}$ 
7:    $y_{shift} \leftarrow -\frac{d_{ball}}{\sqrt{3}}$ 
8:    $M \leftarrow \text{ceil}(\frac{2R_{net}}{\min([x_{scale}, y_{scale}, z_{scale}])})$ 
9:    $counter \leftarrow 0$ 
10:  for  $i \leftarrow 1$  to  $M$  do
11:    for  $j \leftarrow 1$  to  $M$  do
12:      for  $k \leftarrow 1$  to  $M$  do
13:         $counter \leftarrow counter + 1$ 
14:         $x[counter] \leftarrow k \times x_{scale}$ 
15:         $y[counter] \leftarrow j \times y_{scale}$ 
16:         $z[counter] \leftarrow i \times z_{scale}$ 
17:        if  $j$  even then
18:           $x[counter] \leftarrow x[counter] + x_{shift}$ 
19:        end if
20:        if  $i$  even then
21:           $y[counter] \leftarrow y[counter] + y_{shift}$ 
22:        end if
23:      end for
24:    end for
25:  end for
26:   $N \leftarrow M^3$  ▷ Total number of nodes in the lattice
27:  return  $(x, y, z), N$ 
28: end function

```

Algorithm 3 Initialising Sphere lattice

Inputs: R_{net} : radius of the spherical lattice r_{ball} : radius of points in the lattice**Outputs:** $(x_1, y_1, z_1), \dots, (x_{N_{net}}, y_{N_{net}}, z_{N_{net}})$: $(x_{sphere}, y_{sphere}, z_{sphere})$ coordinates of nodes $r_1, \dots, r_{N_{net}}$: r_{sphere} radii of nodes N_{net} number of nodes in the spherical lattice

```

1: function ESTABLISHSPHERELATTICE( $R_{net}, r_{ball}$ )
2:    $(x, y, z), N \leftarrow \text{ESTABLISHHCP LATTICE}(R_{net}, r_{ball})$ 
3:    $x \leftarrow x - \text{mean}(x)$  ▷ demean vector x
4:    $y \leftarrow y - \text{mean}(y)$  ▷ demean vector y
5:    $z \leftarrow z - \text{mean}(z)$  ▷ demean vector z
6:    $r \leftarrow \sqrt{x^2 + y^2 + z^2}$  ▷ compute norm over all points
7:    $counter \leftarrow 0$ 
8:   for  $i \leftarrow 1$  to  $N$  do
9:     if  $r[i] \leq R_{net}$  then ▷ Find members of hcp-lattice within sphere radius  $R_{net}$ 
10:       $counter \leftarrow counter + 1$ 
11:       $x_{sphere}[counter] \leftarrow x[i]$ 
12:       $y_{sphere}[counter] \leftarrow y[i]$ 
13:       $z_{sphere}[counter] \leftarrow z[i]$ 
14:       $r_{sphere}[counter] \leftarrow r[i]$ 
15:    end if
16:  end for
17:   $N_{net} \leftarrow counter$  ▷ Define number of nodes within the spherical domain
18:  return  $(x_{sphere}, y_{sphere}, z_{sphere}), r_{sphere}, N_{net}$ 
19: end function

```

Algorithm 4 Initialising lattice

Inputs: R_{net} : radius of the spherical lattice r_{ball} : radius of points in the lattice**Outputs:** $(x_1, y_1, z_1), \dots, (x_N, y_N, z_N)$: (x, y, z) coordinates of nodes r_1, \dots, r_N : r radial coordinate of nodes $K \in \mathbb{R}^N \times \mathbb{R}^N$: connectivity matrix

```

1: function ESTABLISHLATTICE( $R_{net}, r_{ball}$ )
2:    $(x, y, z), r, N \leftarrow \text{ESTABLISHSPHERELATTICE}(R_{net}, r_{ball})$ 
3:    $d_{ball} \leftarrow 2r_{ball}$ 
4:   for  $i \leftarrow 1$  to  $N$  do
5:     for  $j \leftarrow 1$  to  $N$  do
6:        $dist \leftarrow \sqrt{(x[i] - x[j])^2 + (y[i] - y[j])^2 + (z[i] - z[j])^2}$ 
7:       if  $dist = d_{ball}$  then
8:          $K[i][j] \leftarrow 1$ 
9:       else
10:         $K[i][j] \leftarrow 0$ 
11:      end if
12:    end for
13:  end for
14:  return  $(x, y, z), r, K$ 
15: end function

```

Algorithm 5 Initialising populations

Inputs:

N : number of nodes in network
 ρ : proportion of population 1 nodes

Outputs:

N_1, N_2 : number of nodes in the respective population 1
 P_1, P_2 : population sets
 \mathcal{A} : network sortedness

```

1: function ASSIGNINITIALPOPULATIONS( $N, \rho$ )
2:    $U \leftarrow$  random permutation of  $\{1, \dots, N\}$ 
3:    $N_1 \leftarrow \text{floor}(\rho N)$ 
4:    $N_2 \leftarrow N - N_1$ 
5:    $P_1, P_2 \leftarrow$  integer array of length  $N_1$ , integer array of length  $N_2$ 
6:   for  $k \leftarrow 1$  to  $N_1$  do
7:      $P_1[k] = U[k]$  ▷ Assign first  $N_1$  elements of  $U$  to  $P_1$ 
8:   end for
9:   for  $k \leftarrow 1$  to  $N_2$  do
10:     $P_2[k] = U[N_1 + k]$  ▷ Assign last  $N_2$  elements of  $U$  to  $P_2$ 
11:  end for
12:   $\mathcal{A} \leftarrow$  network sortedness value (3) using  $P_1$  and  $P_2$ 
13:  return  $N_1, N_2, P_1, P_2, \mathcal{A}$ 
14: end function

```

Algorithm 6 Defining node pair selection probabilities

Inputs:

r_1, \dots, r_N : radial coordinates of nodes
 N_1, N_2 : number of nodes in the respective population
 P_1, P_2 : population sets

Outputs:

$f \propto$ probability density function for node pair selection
 $F \propto$ cumulative density function for node pair selection
 Q : normalisation constant for f

```

1: function COMPUTESELECTIONPROBABILITIES( $r[], N_1, N_2, P_1, P_2$ )
2:    $f \leftarrow$  array of length  $N_1 \times N_2$ ,
3:    $F \leftarrow$  array of length  $N_1 \times N_2 + 1$ 
4:    $F[1] \leftarrow 0$ 
5:    $k, Q \leftarrow 0$ 
6:   for  $i \leftarrow 1$  to  $N_1$  do
7:     for  $j \leftarrow 1$  to  $N_2$  do
8:        $k \leftarrow k + 1$ 
9:        $p \leftarrow 1/R_{n_i, P_1} \times 1/R_{n_j, P_2}$  ▷ Weight probability of node pair being selected using (7)
10:       $f[k] = p$ 
11:       $Q \leftarrow Q + p$ 
12:       $F[k] \leftarrow Q$ 
13:    end for
14:  end for
15:  return  $f, F, Q$ 
16: end function

```

Algorithm 7 Node population swapping

Inputs:

$f \propto$ probability density function for node pair selection
 $F \propto$ cumulative density function for node pair selection
 Q : normalisation constant for f
 P_1, P_2 : sets of indices of nodes in the respective population

Outputs:

\tilde{P}_1, \tilde{P}_2 : population sets following node population swap
 \mathcal{A}_p : network sortedness of network with node populations swapped
 k : index of node pair swapped

```

1: function NODESWAP( $f, F, Q, N_1, N_2, P_1, P_2$ )
2:    $u \leftarrow U(0, 1)$  ▷ Sample from unit uniform distribution
3:    $k \leftarrow 1$ 
4:   while  $u < F(k)/Q$  do
5:      $k \leftarrow k + 1$ 
6:   end while
7:    $i, j \leftarrow k/N_2, (k - 1) \bmod N_2 + 1$  ▷ Indices of selected population nodes
8:    $\tilde{P}_1, \tilde{P}_2 \leftarrow P_1, P_2$  ▷ Create copies of  $P_1$  and  $P_2$ 
9:    $\tilde{P}_1(i), \tilde{P}_2(j) \leftarrow P_2(j), P_1(i)$  ▷ Trial node population swap
10:   $\mathcal{A}_p \leftarrow$  network sortedness value (3) using  $\tilde{P}_1$  and  $\tilde{P}_2$ 
11:  return  $\tilde{P}_1, \tilde{P}_2, \mathcal{A}_p, k$ 
12: end function

```

D. Evaluation of collective dynamics

For each node, the number of peaks was identified by searching for maxima exceeding $0.01 \mu M$ in the Ca^{2+} timecourse across the simulation duration (see Fig. S1).

For a network with N nodes, the time-dependent Kuramoto order parameter is a complex-valued scalar defined as

$$z(t) = R(t)e^{i\Theta(t)} = \frac{1}{N} \sum_{j=1}^N e^{i\theta_j(t)}, \quad (\text{S13})$$

where $\theta_j(t)$ is the phase of the j th node, as extracted via a mean-subtracted Hilbert transform of the Ca^{2+} signal for node j . The argument of z , Θ , is the mean phase of the network whilst its magnitude, R , measures the degree of synchrony across the network. We sample the Ca^{2+} at equispaced time points $t_i = i\delta t$, $i = 0, \dots, T-1$ and record the time-averaged degree of synchronisation: $\bar{R} = \frac{1}{T} \sum_{i=0}^{T-1} R(t_i)$.

E. The swapping algorithm generally converges to a single cluster of population 1 nodes

We first ran Algorithm 1 1,000 times in configurations where nodes from population 1 accounted for 10% of the network (i.e., $N_1 = 102$ and $N_2 = 916$). The initial networks ($a = 0$) were uniform-randomly distributed ($\mathcal{A}_{init} = -9.37E - 4 \pm 0.012$), and the algorithm was run until it reached convergence ($a = a_{final}$). Fig. S2 shows five examples (one per column) at several iterations between uniformly random spatial distribution ($a = 0$) and convergence ($a = a_{final}$). We found that convergence took 227.75 ± 40.34 iterations (Fig. S4E) and the final network sortedness was $\mathcal{A}_{final} = 0.69 \pm 0.019$. Fig. S4A shows examples of the relationship between \mathcal{A} and a for individual runs of the swapping algorithm (grey lines) as well as the average \pm standard deviation (blue lines) over all the runs.

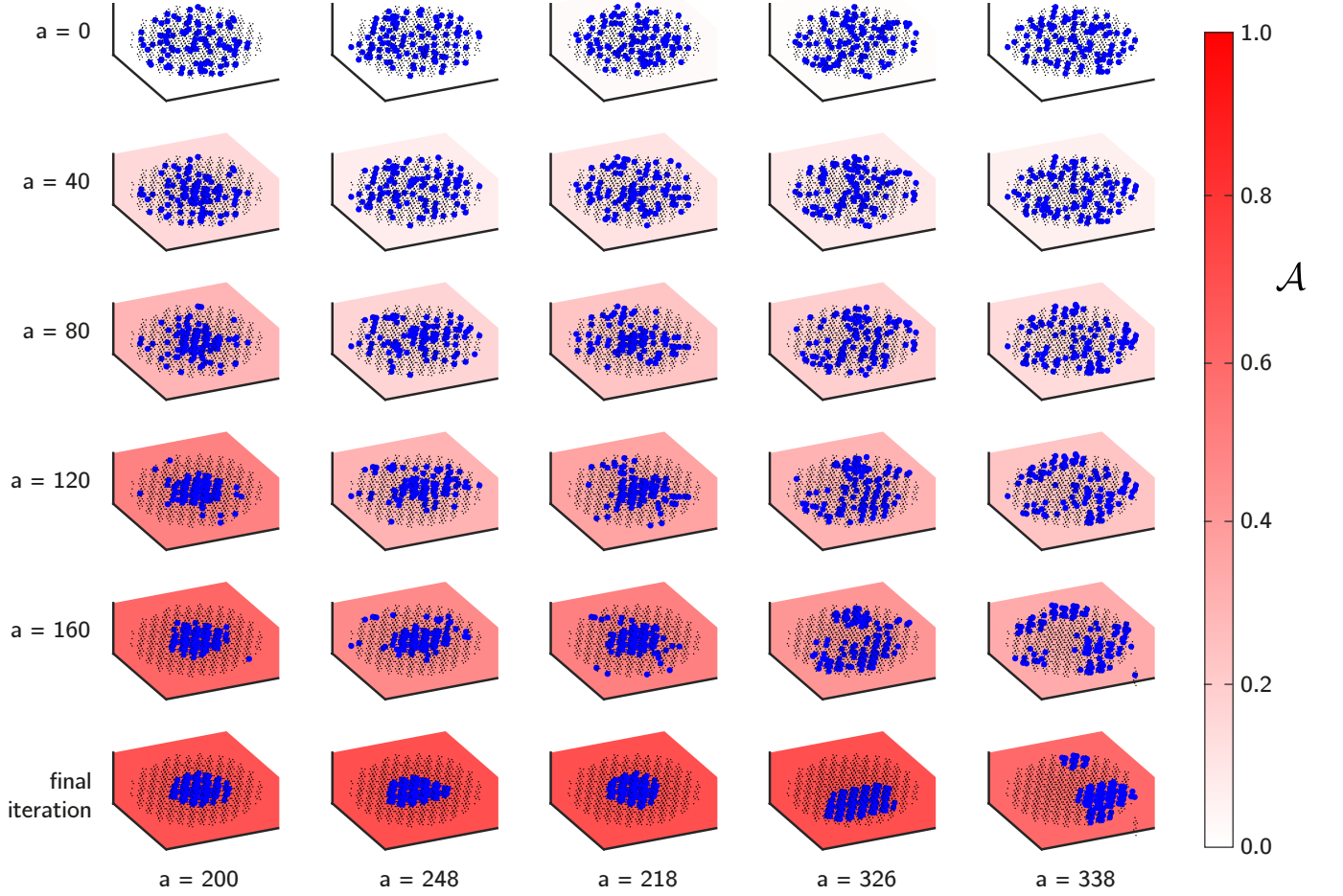


Figure S2. **Examples of the swapping algorithm.** Five examples of the forward swapping algorithm and the associated \mathcal{A} values. The final row of panels shows the final iteration, when no increases in \mathcal{A} are possible. Population 1 nodes are 10% of the total number of nodes and are shown in blue. Population 2 is shown in black. Generally, population 1 forms a single cluster as the algorithm converges, however this is not always the case (see example 5).

For each run, we determined the number of population 1 clusters (or connected components) as a function of iterations a . We found that the population 1 nodes were initially separated into 56.02 ± 4.86 connected components (C_{init}) at $a = 0$. In 96.3% of cases, population 1 formed a single cluster at $a = a_{final}$. The first four columns in Fig. S2 show cases where population 1 converged to a single cluster. In the remaining 3.7% of cases, the population 1 nodes formed multiple clusters at convergence. One such examples of this is displayed in the fifth column in Fig. S2, in which the final network consisted of three clusters. Across all runs, we found that the number of population 1 clusters at convergence was two, three, and four in 2.4%, 1.2%, and 0.1% of runs, respectively. Fig. S4C shows examples of the relationship between number of population 1 clusters and a (grey lines) as well as the average \pm standard deviation (blue lines) over all the runs.

We next ran the backward algorithm 1,000 times when population 1 formed 10% of the network nodes. Fig. S3 shows five examples (one per column) at several iterations between uniform-random spatial distribution ($a = 0$) and convergence ($a = a_{final}$). We found that convergence took 202.68 ± 14.58 iterations and the final network sortedness

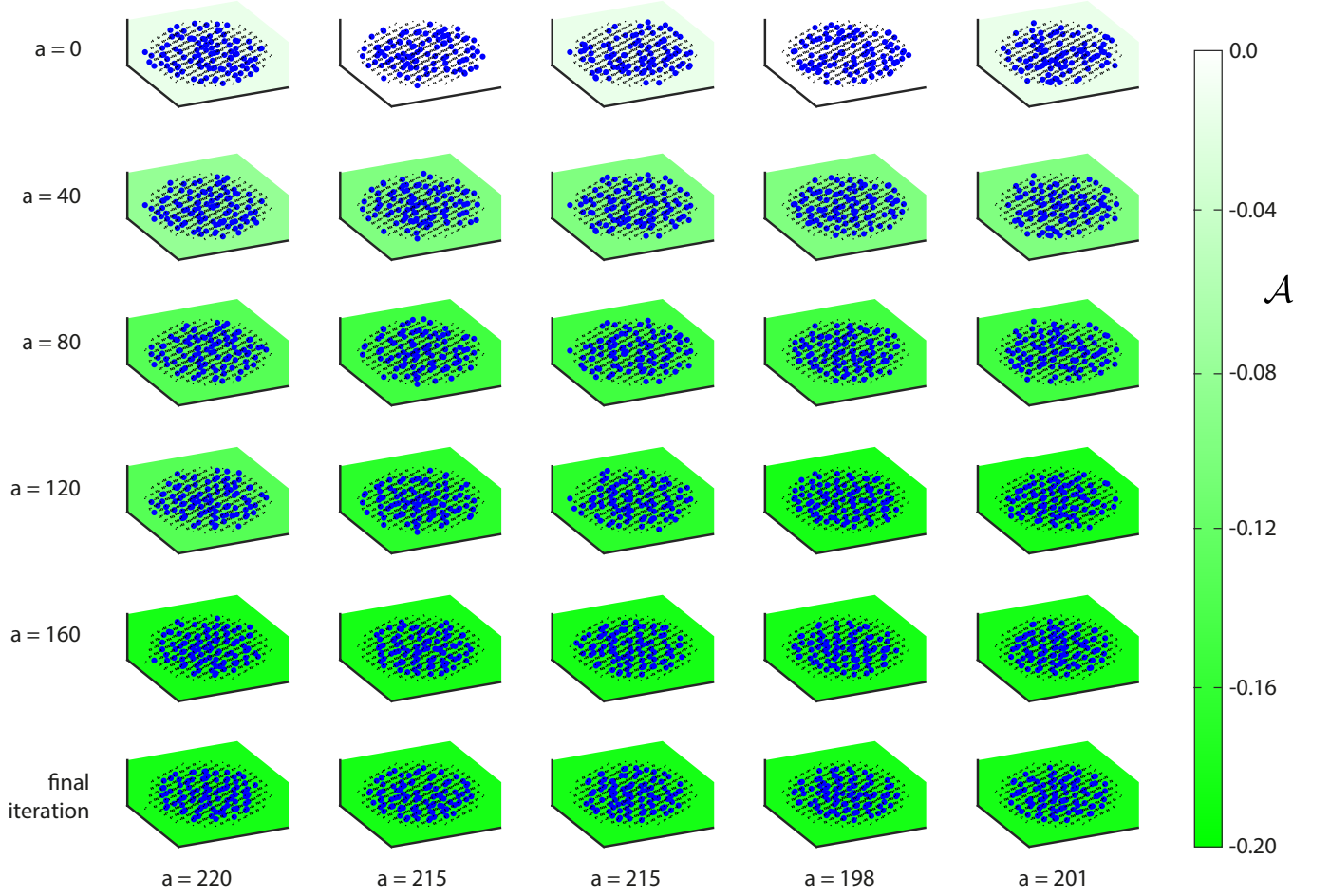


Figure S3. **Examples of the backward swapping algorithm.** Five examples of the backward swapping algorithm and the associated \mathcal{A} values. The final row of panels shows the final iteration, when no decreases in \mathcal{A} are possible. Population 1 nodes account for 10% of the total number of nodes and are shown in blue. Population 2 is shown in black. Generally, all population 1 nodes become isolated as the algorithm converges.

N_1	N_2	direction	a_{final}	\mathcal{A}_{final}	C_{init}	C_{final}
102	916	+1	227.75 ± 40.34	0.69 ± 0.019	56.02 ± 4.86	1.05 ± 0.28
102	916	-1	202.68 ± 14.58	-0.11 ± 0.00	56.02 ± 4.86	102 ± 0
204	814	+1	382.36 ± 56.12	0.72 ± 0.0060	46.33 ± 5.95	1.01 ± 0.095
204	814	-1	401.41 ± 24.48	-0.22 ± 0.0029	46.33 ± 5.95	203.97 ± 0.29

Table S2. Swapping algorithm statistics where population 1 comprises 10% and 20% of the network.

was $\mathcal{A}_{final} = -0.11 \pm 0.00$. In addition, the number of connected components at a_{final} was 102 in each case. This is because the algorithm always reached a state in which all population 1 cells were isolated from one another (i.e., these nodes were coupled only to nodes from population 2). Finally, we ran the forward and backward algorithm again 1,000 times when population 1 comprised 20% of the network (i.e., $N_1 = 204$ and $N_2 = 814$). The statistics for each of these cases are reported in Table S2. In Fig. S4B, we show the average relationship between \mathcal{A} and a and Fig. S4D shows the average relationship between population 1 clusters and a over all runs for each case.

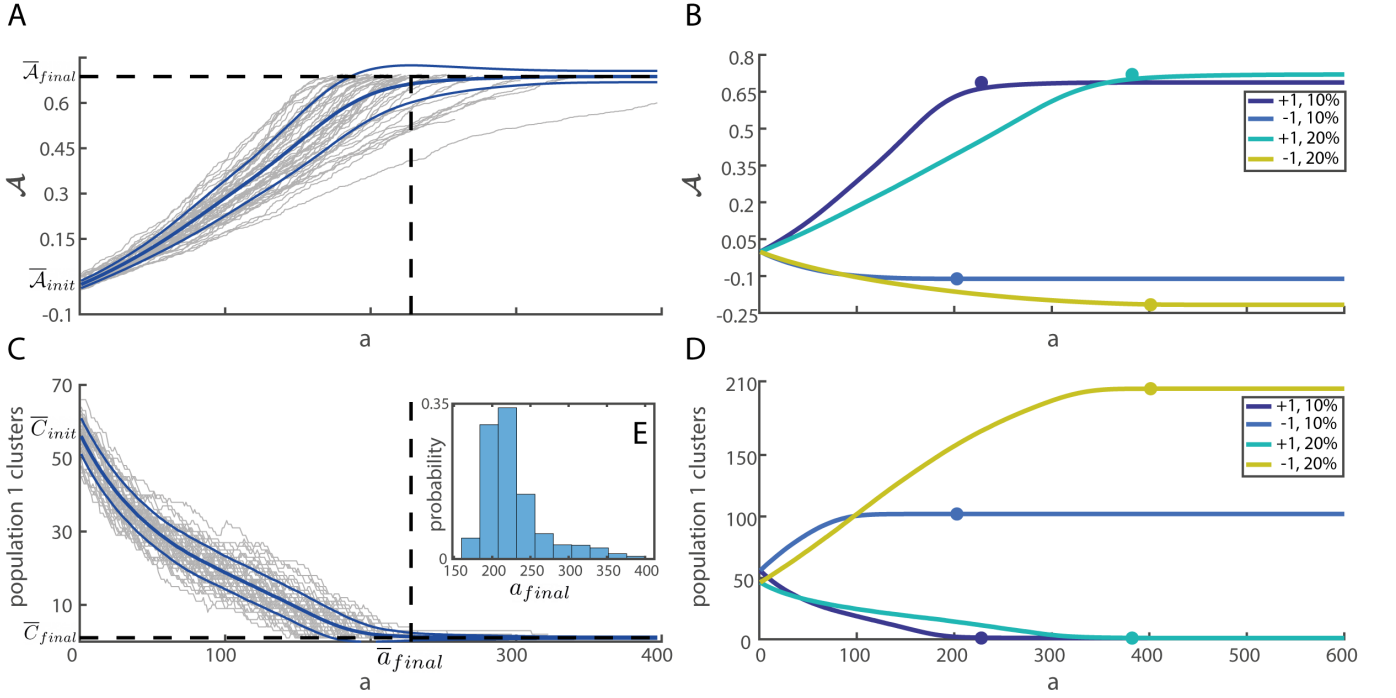


Figure S4. **Convergence of the swapping algorithm.** **A)** The relationship between \mathcal{A} and a is shown for a subset of the 1,000 runs of Algorithm 1 (grey lines). Population 1 was 10% of the total number of nodes in the network. The average \pm standard deviation is shown as blue lines. $\bar{\mathcal{A}}_{init} = -9.37E - 4$ was the mean value \mathcal{A} when $a = 0$ over all runs. $\bar{\mathcal{A}}_{final} = 0.69$ was the mean value of \mathcal{A} when $a = a_{final}$ over all runs. $\bar{a}_{final} = 227.75$ was the mean value of a at a_{final} over all runs. **B)** The relationship between population 1 clusters and a is shown for a subset of the 1,000 runs of Algorithm 1 (grey lines). Population 1 was 10% of the total number of nodes in the network. The average \pm standard deviation is shown as blue lines. $\bar{C}_{init} = 56.02$ was the average number of population 1 clusters at $a = 0$ over all runs. $\bar{C}_{final} = 1.05$ was the average number of population 1 clusters at $a = a_{final}$ over all runs. **C)** The relationship between \mathcal{A} and a for the forward and backward algorithm when population 1 was 10% and 20% of the overall network. The average over all runs is plotted for each case. Each curve also has a point of the same colour which indicates $(\bar{a}_{final}, \bar{\mathcal{A}}_{final})$. **D)** The relationship between population 1 clusters and a for the forward and backward algorithm when population 1 was 10% and 20% of the overall network. The average over all runs is plotted for each case. Each curve also has a point of the same colour which indicates $(\bar{a}_{final}, \bar{\mathcal{A}}_{final})$. **E)** An inset showing the distribution of a_{final} over the 1,000 runs when population 1 was 10% of the network and the algorithm was run in the forward direction.

F. The relationship between drive and sortedness with respect to network synchronisation and activation across many initial seeds of the sorting algorithm

In section III A, we characterised the behaviours displayed by the networks defined by the population sets \mathcal{P}_1 and \mathcal{P}_2 for $G \in [0.3, 0.55]$ (the interval over which cells in population 1 are intrinsically active, whilst those in population 2 are not). We found that for strong coupling ($g_{coup} = 10$), the threshold for activation and synchronisation of the full network is strongly dependent on \mathcal{A} , such that increasing \mathcal{A} decreases the necessary drive G for transition (see Sec. III A 1). For $g_{coup} \in \{1, 2\}$, we found several regimes of activity, as described in Sec. III A 2 and Sec. III A 3. Here, we wish to establish if the identified domains of activity persist across general families of networks with similar

\mathcal{A} but different membership of the population sets.

To do this, we defined ranges for the extracellular glucose concentration $G \in [0.3, 0.55]$ and for the number of network iterations $a \in [0, 250]$ ($a \in [0, 400]$ when $N_1/N \approx 0.2$). We selected $M = 2,048$ points in the (a, G) plane over these ranges following a Latin hypercube sampling. For each realisation $m \in \mathbb{N}_M$, we ran Algorithm 1 for a_m iterations and recorded the modified spatial sortedness value \mathcal{A}_m . For maximum coverage over the range of possible values of \mathcal{A} , Algorithm 1 was run in either a forward or a backward fashion (see Sec. II C). We did this by selecting the Algorithm direction $d_m \in \{-1, 1\}$ randomly and with uniform probability. Once the algorithm terminated, the dynamics (S1)-(S11) of the resulting network configuration were simulated using the chosen activation value G_m and the summary statistics as described in Sec. II D were evaluated. These summary statistics were then plotted against the set of (\mathcal{A}_m, G_m) values. We then repeated this process for different values of g_{coup} and proportions of population 1 nodes $N_1 = 102$ ($N_1/N \approx 0.1$) (as in the Sec. III A) and $N_1 = 204$ ($N_1/N \approx 0.2$).

Evaluation of the level sets led to complicated sets due to the use of different realisations of Algorithm 1 and the use of different initial conditions. Since the complex nature of these level sets was not related to the relationship between sortedness, drive, and network dynamics, and further because it obfuscated results, we opted to remove these portions of the levels sets from Figs. S5- S7. As an example for comparison, Fig. S17 includes the full level sets corresponding to Fig. S7A.

1. *Increasing \mathcal{A} lowers the required drive G for a transition to globally synchronised bursting for strong coupling and varying population sizes*

We found that the monotonic decreasing relationship between \mathcal{A} and G discussed in Sec. III A 1 persists when each point (\mathcal{A}_m, G_m) corresponds to a different realisation of the swapping algorithm. The regimes \mathcal{D}^- and \mathcal{D}^+ both exist and can be separated by the same level sets as defined previously: $L^* = \{(\mathcal{A}, G) \mid \bar{R}(\mathcal{A}, G) = 0.9\}$, and $L^+ = \{(\mathcal{A}, G) \mid \bar{P}(\mathcal{A}, G) = 5\}$. These boundaries show a decreasing trend in G with respect to \mathcal{A} in the transition from global quiescence to globally synchronised oscillations, although due to each point representing a different realisation of the Algorithm 1 (and a distinct set of initial conditions), the separatrix is now non-monotonic. Fig. S5 shows \bar{P} and \bar{R} when population 1 nodes account for 10% (Fig. S5A,B) of the network and for 20% (Fig. S5C,D) of the network. We found that increasing the proportion of population 1 nodes did not change the nature of the relationship between \mathcal{A} and G , however, the threshold for activation G was decreased over all values of \mathcal{A} . This decrease in threshold is expected as the number of intrinsically active nodes (and hence ‘intrinsic’ network excitability) in the network was doubled.

2. *The regime of inter-population resonance persists across realisations of the swapping algorithm for middle-strength coupling*

For intermediate-strength coupling ($g_{\text{coup}} = 2$), we found that the regimes discussed in Sec. III A 2 still exist when each point (\mathcal{A}_m, G_m) corresponds to a different realisation of the swapping algorithm. In particular, we found the existence of the regions \mathcal{D}^- , \mathcal{D}^+ , and \mathcal{D}^* , which can be separated by the level sets L_1^+ and L_2^+ , where $L_k^+ = \{(\mathcal{A}, G) \mid \bar{P}_k(\mathcal{A}, G) = 5\}$ for $k \in \{1, 2\}$, can be used to separate the three regimes. Moreover, we observed some network

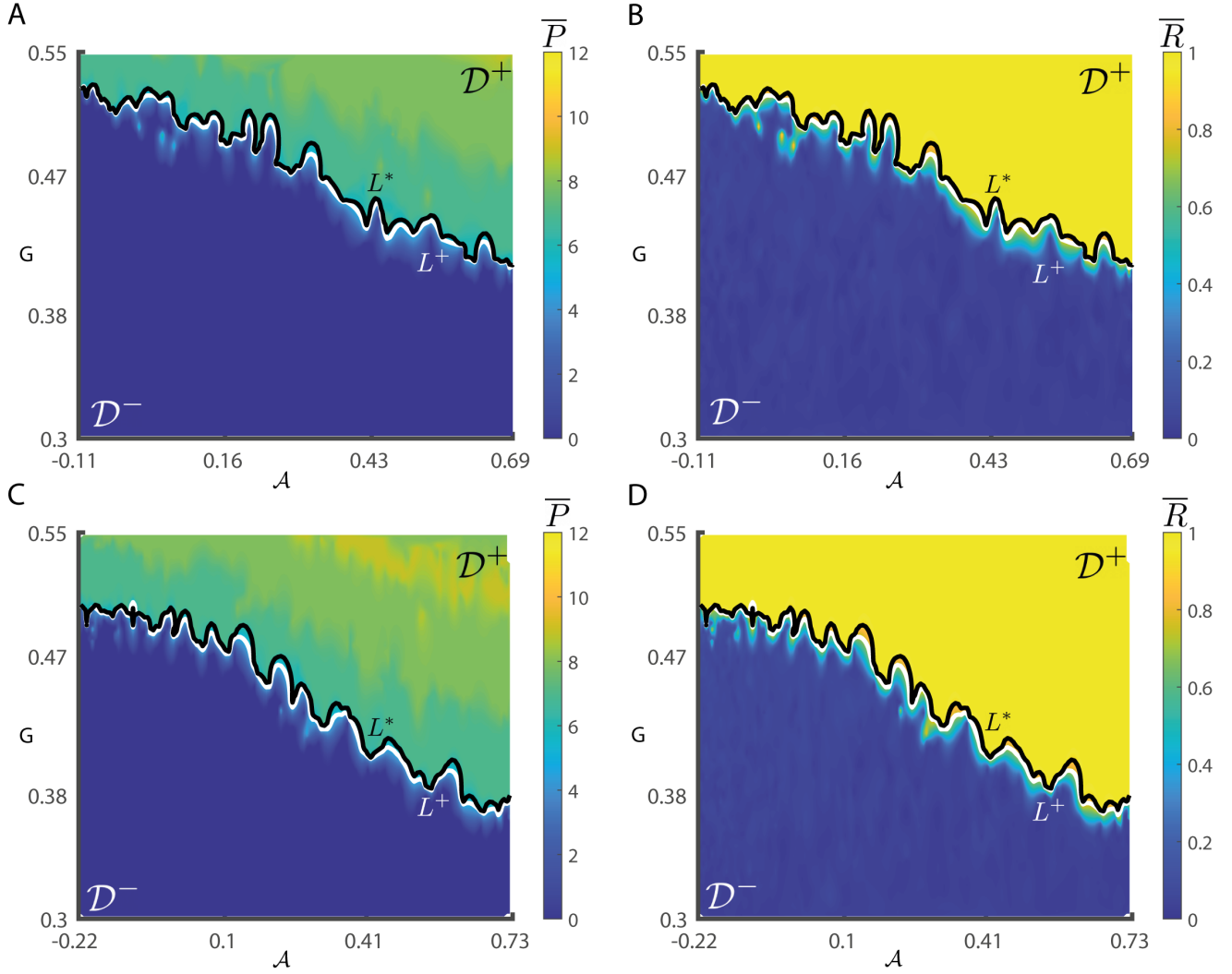


Figure S5. **Network activity with respect to sortedness and drive for strong coupling across realisations of the swapping algorithm.** **A)** Plotting \bar{P} on a set of realisations of the swapping algorithm, (\mathcal{A}_m, G_m) , shows a decreasing trend in necessary drive with respect to \mathcal{A} for activation. In this case, population 1 was 10% of the network. **B)** Plotting \bar{P} on a set of realisations of the swapping algorithm, (\mathcal{A}_m, G_m) , shows a decreasing trend in necessary drive with respect to \mathcal{A} for synchronisation. In this case, population 1 was 10% of the network. **C)** As in A, but where population 1 was 20% of the network. **D)** As in B, but where population 1 was 20% of the network.

simulations which exhibited lowered \bar{R} within \mathcal{D}^+ , which we conjecture is the result of multi-stability (i.e., different asymptotic dynamics for different initial conditions), as in Fig. S14. Figure S6 shows \bar{P} and \bar{R} in the case when population 1 nodes comprise 10% (Fig. S6A,B) and 20% (Fig. S6C,D) of the network. As in the case for strong coupling, each regime is shifted downward, with respect to G , when the proportion on intrinsically active nodes is increased to 20%. In fact, we found that for high degrees of sortedness, the inter-population resonance regime begins at the lowest value of G that we considered ($G = 0.3$). This shows that for middle-strength coupling, high sortedness, and where 20% of the network are nodes from population 1, activation of the network occurs for values of G very near where the threshold ($G \approx 0.25$) at which isolated population 1 nodes become active.

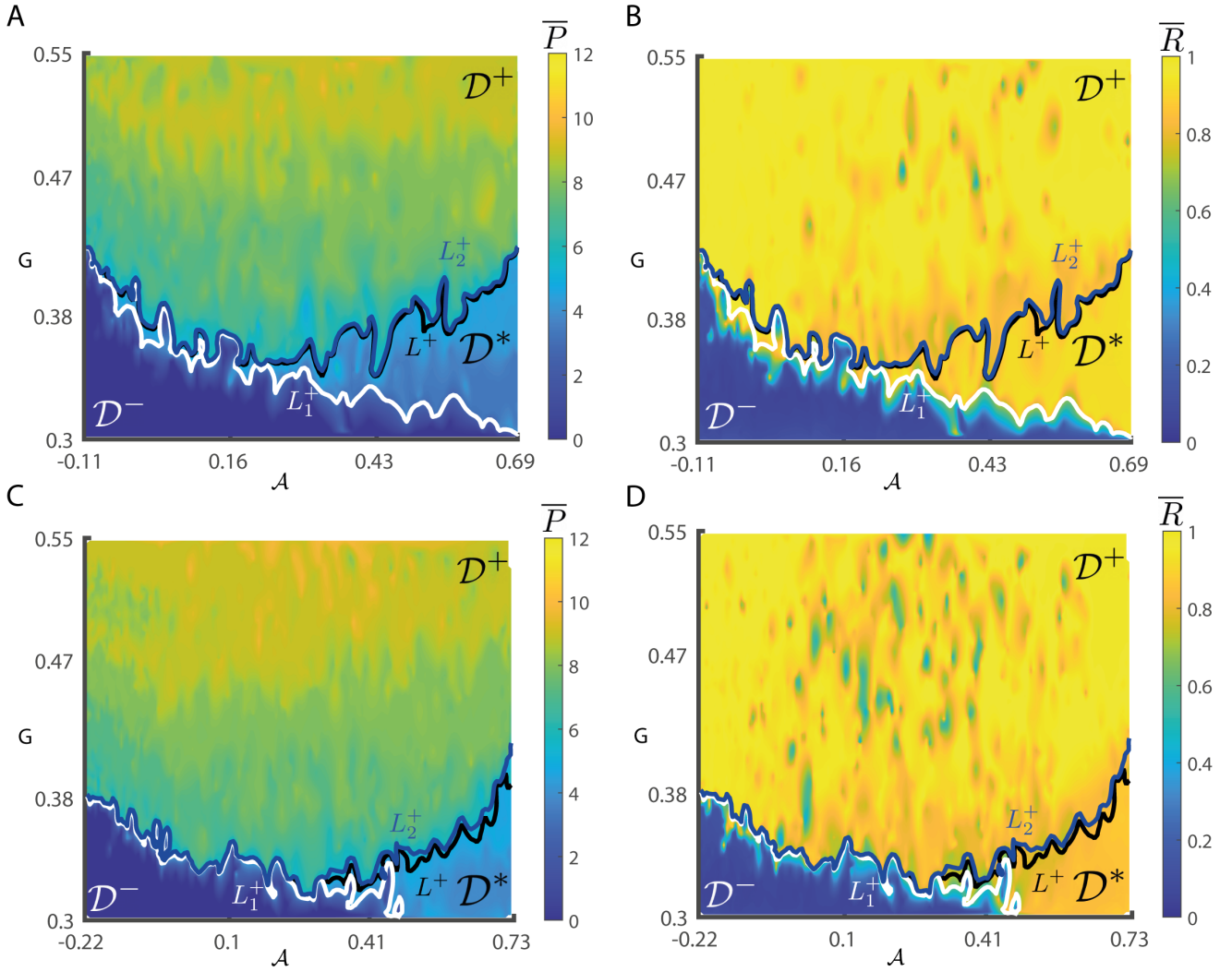


Figure S6. **Network activity with respect to sortedness and drive for middle-strength coupling across realisations of the swapping algorithm.** **A)** Plotting \bar{P} shows that \mathcal{D}^* persists across realisations of the swapping algorithm. In this case, population 1 was 10% of the network. **B)** Plotting \bar{R}_1 shows that \mathcal{D}^* persists across realisations of the swapping algorithm. In this case, population 1 was 10% of the network. **C)** As in A, but where population 1 was 20% of the network. **D)** As in B, but with where population 1 was 20% of the network.

3. *Non-monotonicity with respect to synchronisation persists for weak coupling across realisations of the swapping algorithm and for differing population 1 sizes*

Finally, we considered weak coupling ($g_{coup} = 1$) for (\mathcal{A}_m, G_m) using M realisations of the swapping algorithm. Figure S7 shows \bar{P} and \bar{R} when population 1 nodes account for 10% (Fig. S7A,B) and 20% (Fig. S7C,D) of the network. We found that non-monotonicity of the boundary to synchronised activity with respect to increasing G was persistent for this weak coupling case. The upper boundary of the inter-population resonance regime (\mathcal{D}^*), given by the set L^{2*} , shows an increasing trend with respect to \mathcal{A} both when population 1 node comprise 10% (Fig. S7B) and 20% (Fig. S7D) of the network. Moreover, we again found that the activation threshold for population 1 nodes with respect to G decreases as \mathcal{A} increases, which is captured by L_1^+ , where $L_k^+ = \{(\mathcal{A}, G) \mid \bar{P}_k(\mathcal{A}, G) = 5\}$ for $k \in \{1, 2\}$.

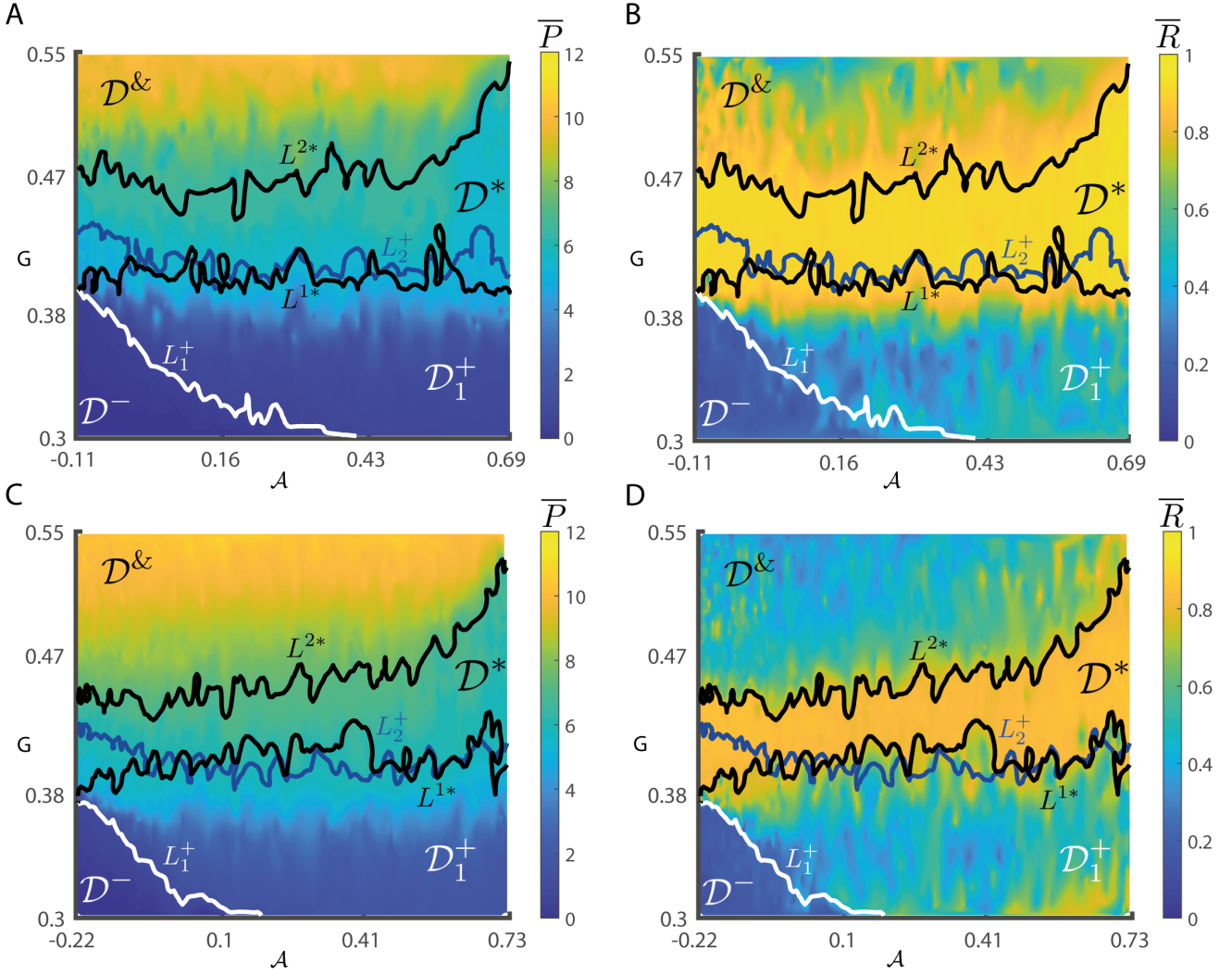


Figure S7. **Network activity with respect to sortedness and drive for weak coupling across realisations of the swapping algorithm.** **A)** Plotting \bar{P} shows that the regimes \mathcal{D}^* and $\mathcal{D}^\&$ persist across realisations of the swapping algorithm. In this case, population 1 was 10% of the network. **B)** Plotting \bar{R}_1 shows that the regimes \mathcal{D}^* and $\mathcal{D}^\&$ persist across realisations of the swapping algorithm. In this case, population 1 was 10% of the network. **C)** As in A, but where population 1 was 20% of the network. **D)** As in B, but where population 1 was 20% of the network.

Interestingly, we found that the activation of population 2 nodes (reflected by L_2^+) with respect to G shows a decreasing trend as \mathcal{A} increases, but only for very low values of \mathcal{A} . We conjecture that this relationship was not observed in Sec. III A 3 because only positive values of \mathcal{A} (resulting from the forward algorithm) were considered there, whereas here we also include realisations of the backward algorithm (leading to negative values of \mathcal{A} being considered). Here, we found that the bounds of \mathcal{D}^* , those being L^{1*} and L^{2*} , needed to be modified depending on the proportion of population 1 nodes in the network. In particular, when only 10% of the network nodes were from population 1, we defined the level set $L^* = \{(\mathcal{A}, G) \mid \bar{R}(\mathcal{A}, G) = 0.9\}$ as in Sec. III A 3 which subsequently led to the definition of two curves: the lower bound L^{1*} and the upper bound L^{2*} (Fig. S7B). However, when the proportion of population 1 nodes was increased to 20%, we instead defined $L^* = \{(\mathcal{A}, G) \mid \bar{R}(\mathcal{A}, G) = 0.8\}$ (Fig. S7D). The thresholds we chose

were dependent on the number of population 2 nodes. This is because we sought to define level sets that bounded the 2:1 resonance region. In that region, nodes are synchronised within, but not between, populations. Therefore, \bar{R} is approximately equal to the fraction of nodes in the larger population (i.e., population 2).

G. Additional figures referenced in the manuscript

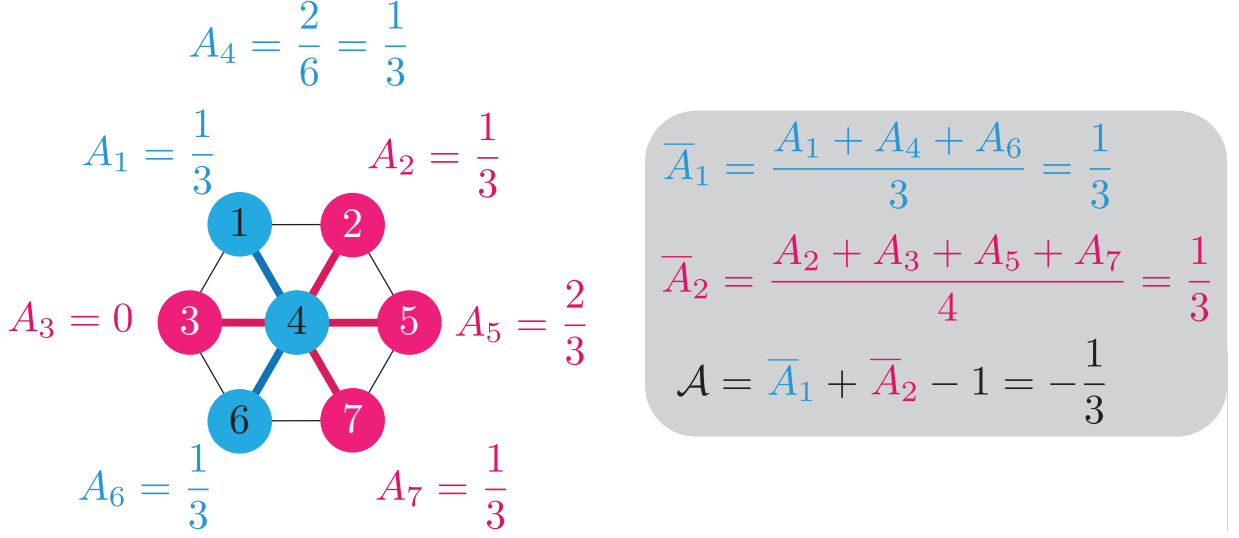


Figure S8. **Illustrative example of network sortedness metric.** The sortedness metrics are computed for the example network comprising $N_1 = 3$ population 1 nodes (blue) and $N_2 = 4$ population 2 nodes (pink) with population sets $P_1 = \{1, 4, 6\}$ and $P_2 = \{2, 3, 5, 7\}$. The node sortedness values, A_i , $i = 1, \dots, 7$, take the indicated values. For ease of viewing one example calculation, the edges of node 4 are highlighted in the colour corresponding to the population of each of its neighbouring nodes. The grey box shows the population sortedness evaluations, \bar{A}_k , $k \in \{1, 2\}$, computed using (2) and overall network sortedness, \mathcal{A} , computed using (3).

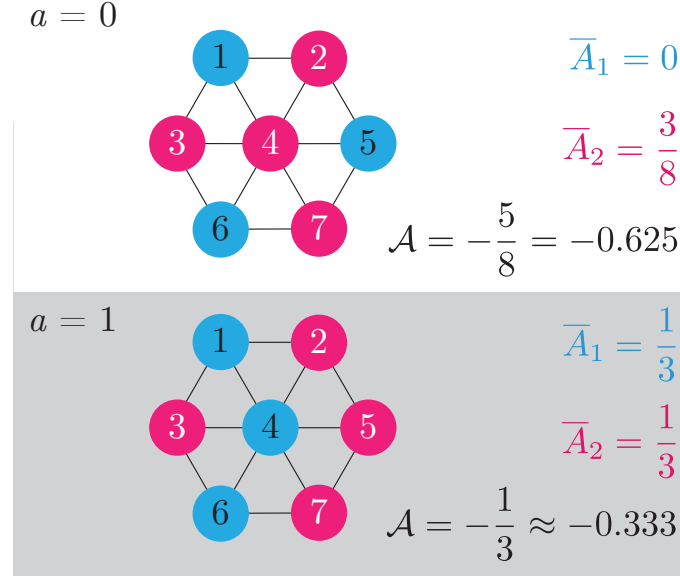


Figure S9. **Example of one iteration of the network sorting algorithm in the forward direction** The initial network with $a = 0$ is in the maximally unsorted state so that no two nodes from population 1 (blue) are coupled to one another. Here, the population sets are $P_1 = \{1, 5, 6\}$ and $P_2 = \{2, 3, 4, 7\}$ and network sortedness is equal to $-5/8$. The algorithm attempts to move node 4 to population 1 and node 5 to population 2 (pink). In the trial configuration shown in the grey box, the network sortedness is equal to $-1/3 > -5/8$ and so the swap is accepted. Thus, the population sets are updated to $P_1 = \{1, 4, 6\}$ and $P_2 = \{2, 3, 5, 7\}$ and the iteration counter is increased to $a = 1$. If the swap were rejected, another pair of nodes would be selected at random and the computation of network sortedness would be repeated. If no possible swap changes \mathcal{A} in the desired direction, the algorithm would terminate without incrementing the iteration number, a .

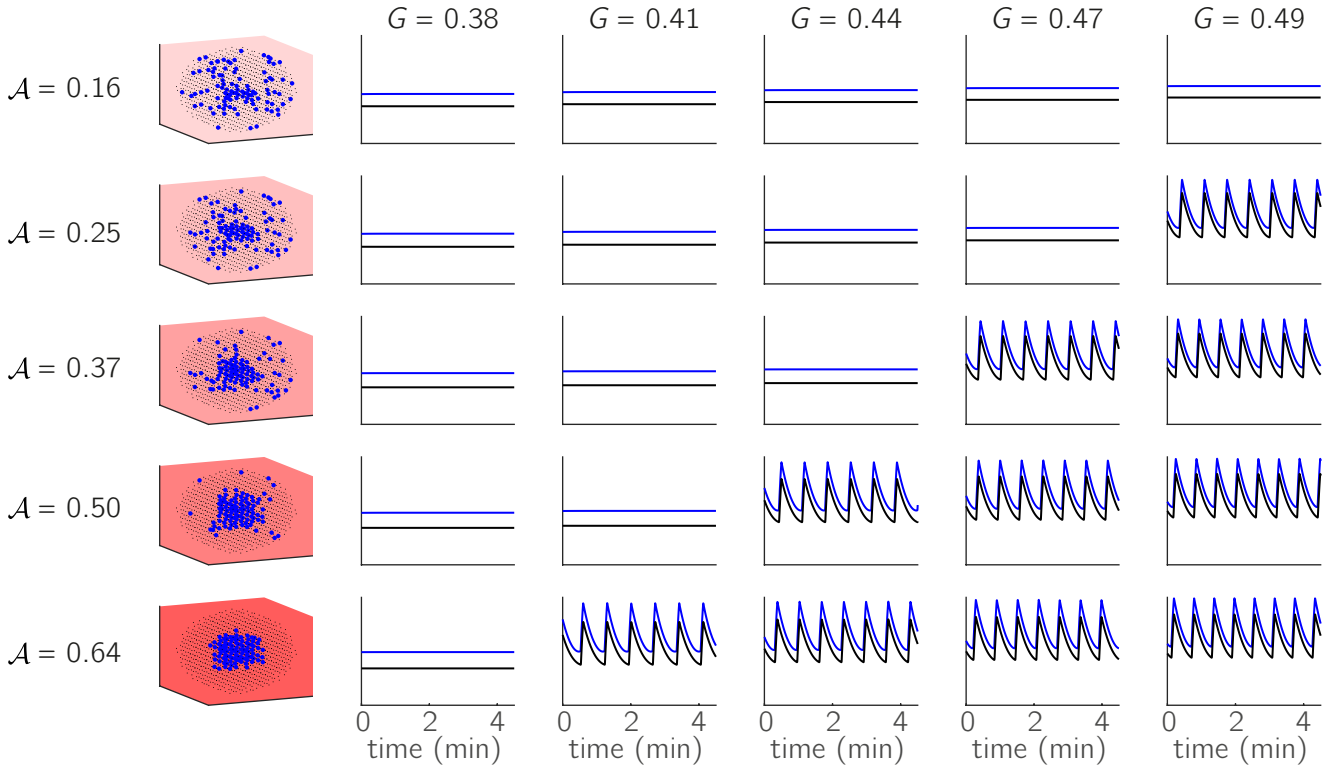


Figure S10. **Phase transitions with respect to spatial sortedness.** The mean Ca^{2+} dynamics of population 1 (blue) and population 2 (black) are shown as \mathcal{A} increases. For higher G , activation occurs at lower \mathcal{A} . Conversely, increasing \mathcal{A} allows weaker G activate the system.

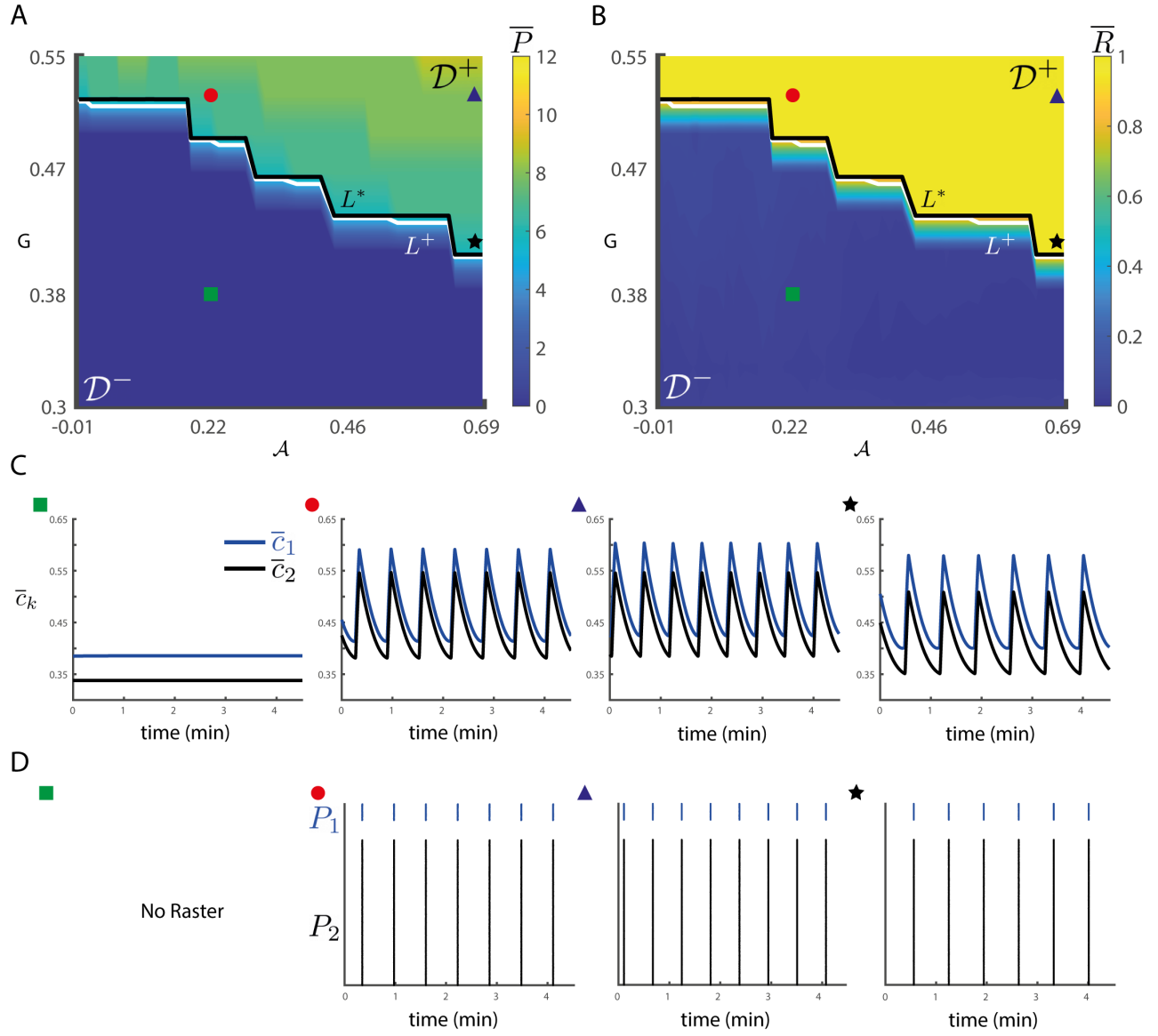


Figure S11. **Network activity with respect to sortedness and drive for strong coupling.** **A)** Plotting \bar{P} averaged over three sets of initial conditions shows that for increasing \mathcal{A} , lower drive G is required to activate the network. **B)** Plotting \bar{R} averaged over three sets of initial conditions shows that for increasing \mathcal{A} , lower drive G is required to synchronise the network. **C)** Average Ca^{2+} across population 1 nodes (\bar{c}_1) and population 2 nodes (\bar{c}_2) for (\mathcal{A}, G) pairs illustrates a strong global signal in \mathcal{D}^+ . **D)** Raster plots showing the strong synchronisation within \mathcal{D}^+ for strong coupling. The raster plot is ordered such that nodes whose indices are in P_1 , i.e. population 1 nodes, are shown in blue at top of the plot, whilst nodes whose indices are in P_2 are shown in black at the bottom of the plot.

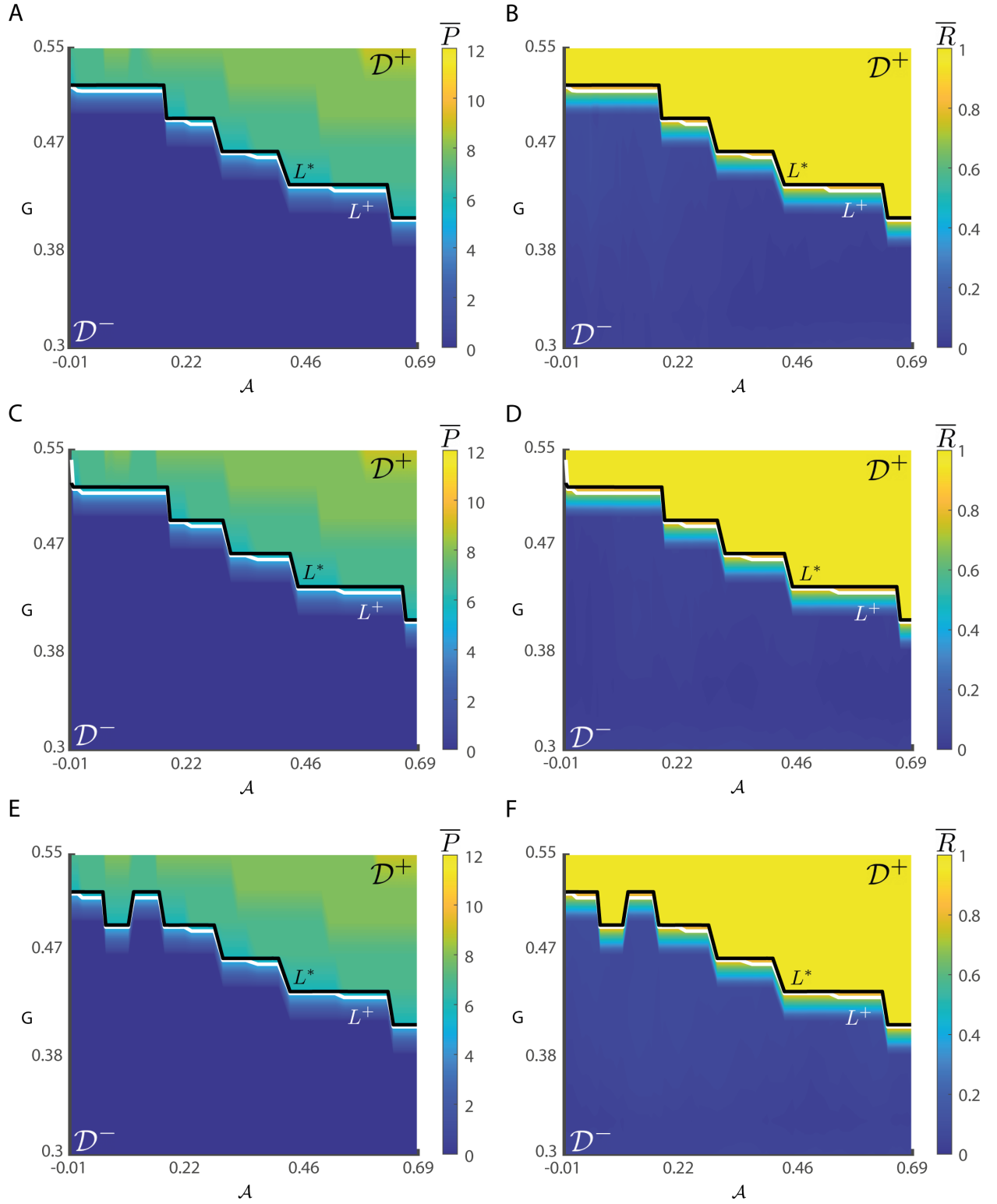


Figure S12. **Network activity with respect to sortedness and drive for strong coupling (three initial conditions).** **A)** Plotting \overline{P} shows that for increasing \mathcal{A} , lower drive G is required to activate the network (parameter set $Y_1(0)$). **B)** Plotting \overline{R}_1 shows that for increasing \mathcal{A} , lower drive G is required to synchronise the network (parameter set $Y_1(0)$). **C)** \overline{P} for $Y_2(0)$. **D)** \overline{R}_1 for $Y_2(0)$. **E)** \overline{P} for $Y_3(0)$. **F)** \overline{R}_1 for $Y_3(0)$.

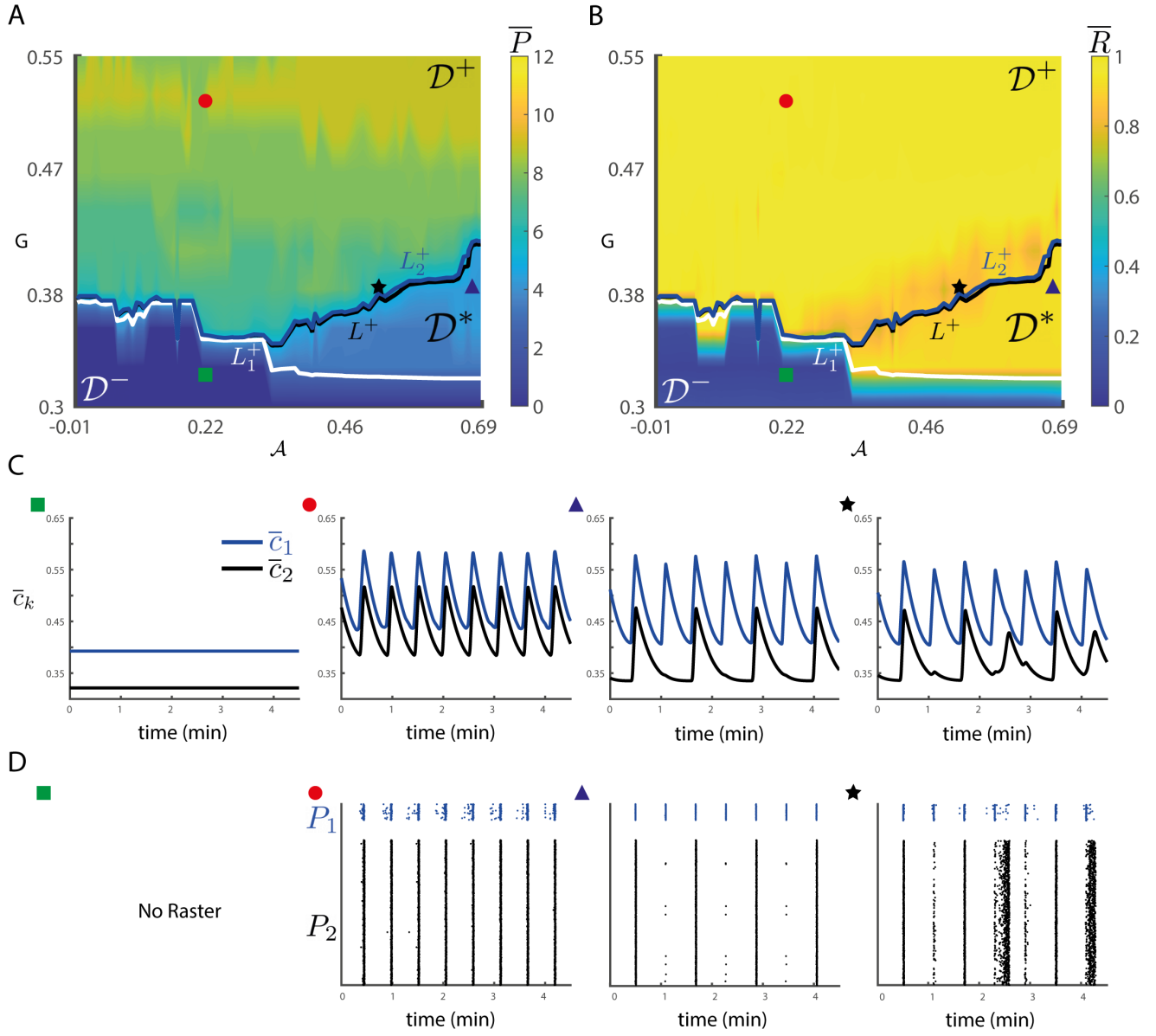


Figure S13. **Network activity with respect to sortedness and drive for middle-strength coupling.** **A)** Plotting \bar{P} averaged over three sets of initial conditions shows a third regime \mathcal{D}^* bounded by L_1^+ and L_2^+ . **B)** Plotting \bar{R}_1 averaged over three sets of initial conditions shows that for increasing A , lower drive G is required to synchronise the network. **C)** Average Ca^{2+} across population 1 nodes (\bar{c}_1) and population 2 nodes (\bar{c}_2) for (A, G) pairs illustrates a strong global signal in \mathcal{D}^+ and that population 2 nodes are active at half the frequency of population 1 nodes, on average, in \mathcal{D}^* . **D)** Raster plots showing the strong synchronisation within \mathcal{D}^+ , 2:1 frequency resonance in \mathcal{D}^* , and intermediate activity with lowered synchronisation in a band separating the two regimes. The raster plot is ordered such that nodes whose indices are in P_1 , i.e. population 1 nodes, are shown in blue at top of the plot, whilst nodes whose indices are in P_2 are shown in black at the bottom.

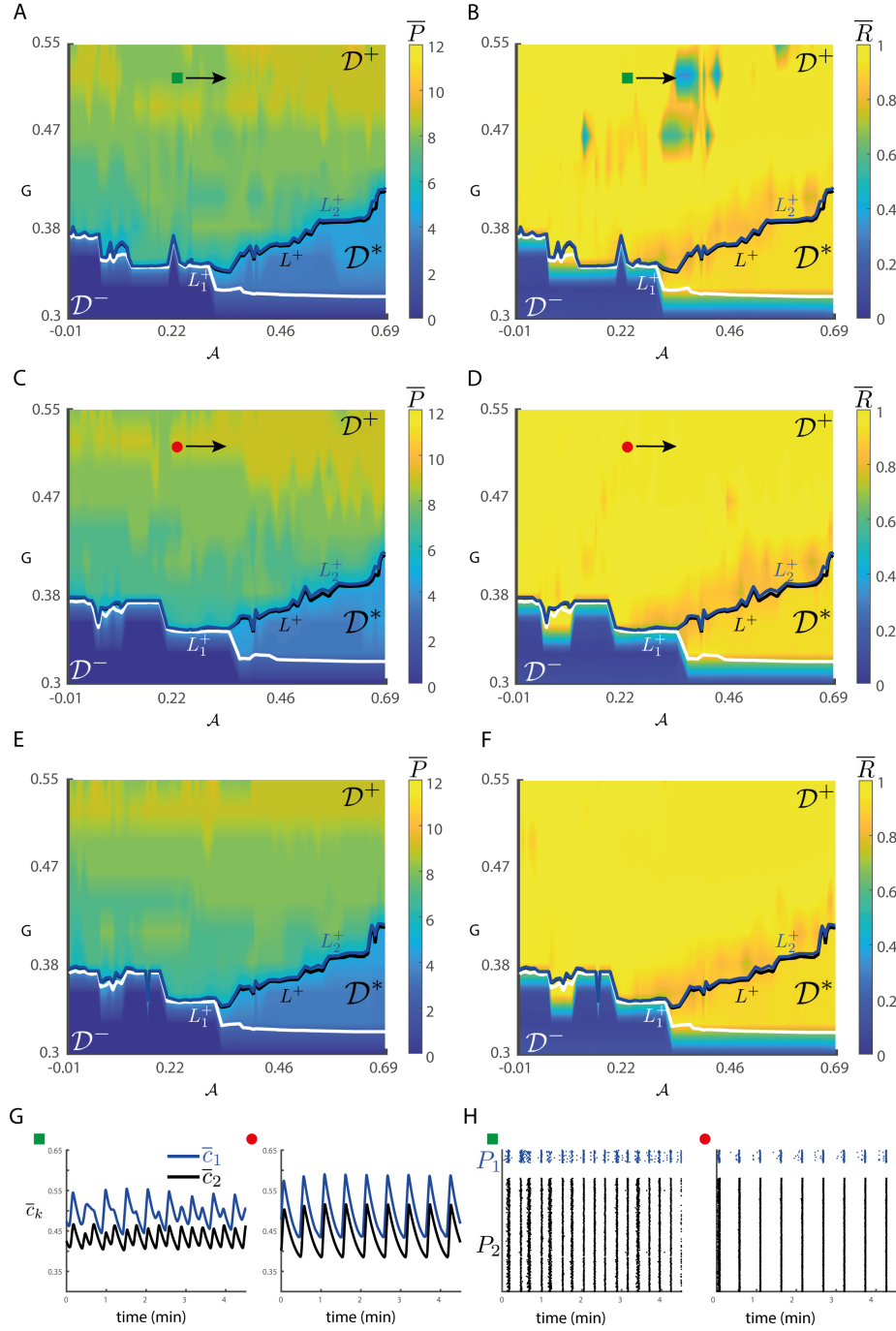


Figure S14. **Network activity with respect to sortedness and drive for middle-strength coupling (three initial conditions).** **A)** \bar{P} for $Y_1(0)$. **B)** \bar{P} for $Y_1(0)$. **C)** \bar{P} for $Y_2(0)$. **D)** \bar{R} for $Y_2(0)$. **E)** \bar{P} for $Y_3(0)$. **F)** \bar{R} for $Y_3(0)$. **G)** Mean Ca^{2+} for P_1 (\bar{c}_1) and P_2 (\bar{c}_2) showing multi-stability in the \mathcal{D}^+ regime. **H)** Raster plots of the population 1 (blue) and population 2 (black) nodes showing multistability in the \mathcal{D}^+ regime. The raster plot is ordered such that nodes whose indices are in P_1 , i.e. population 1 nodes, are shown at the top of the plot.

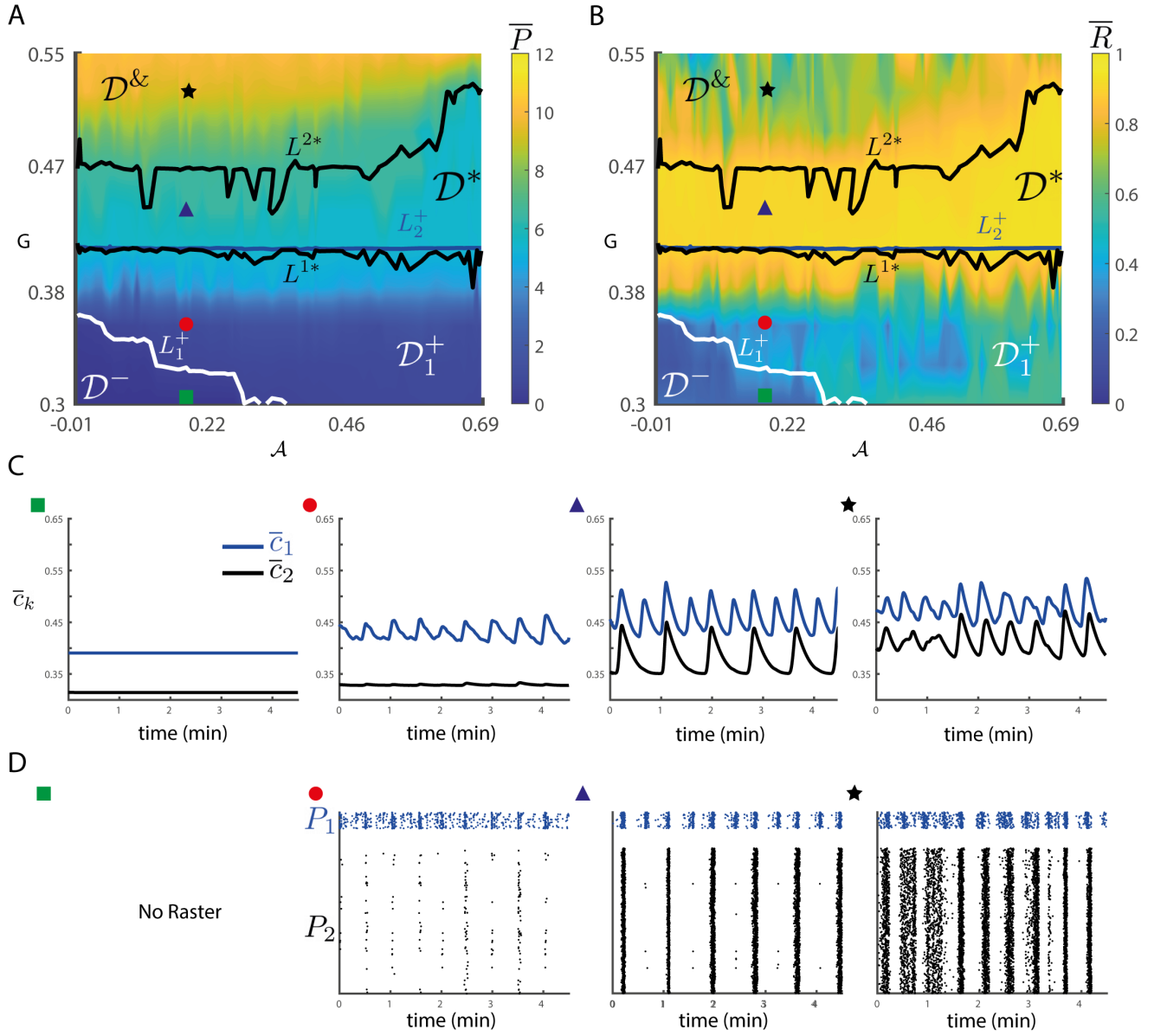


Figure S15. **Network activity with respect to sortedness and drive for weak coupling.** **A)** Plotting \bar{P} averaged over three sets of initial conditions shows that activation of population 1, but not population 2, is dependent on sortedness. **B)** Plotting \bar{R} averaged over three sets of initial conditions shows that synchronisation is non-monotonic with respect to G , peaking within a 2 : 1 resonance regime D^* . **C)** Average Ca^{2+} for population 1 nodes (\bar{c}_1) and population 2 nodes (\bar{c}_2) for (A, G) shows that population 1 is active but only generates a weak global signal in D_1^+ . The dynamics exhibit 2:1 resonance within the region D^* , and lowered coordination and an irregular global signal within $D^\&$. **D)** Raster plots showing the weak coordination of spiking activity across population 1 in D_1^+ and weak coordination of spiking activity across the whole network within $D^\&$. The raster plot is ordered such that nodes whose indices are in P_1 , i.e. population 1 nodes, are shown in blue at top of the plot, whilst nodes whose indices are in P_2 are shown in black at the bottom.

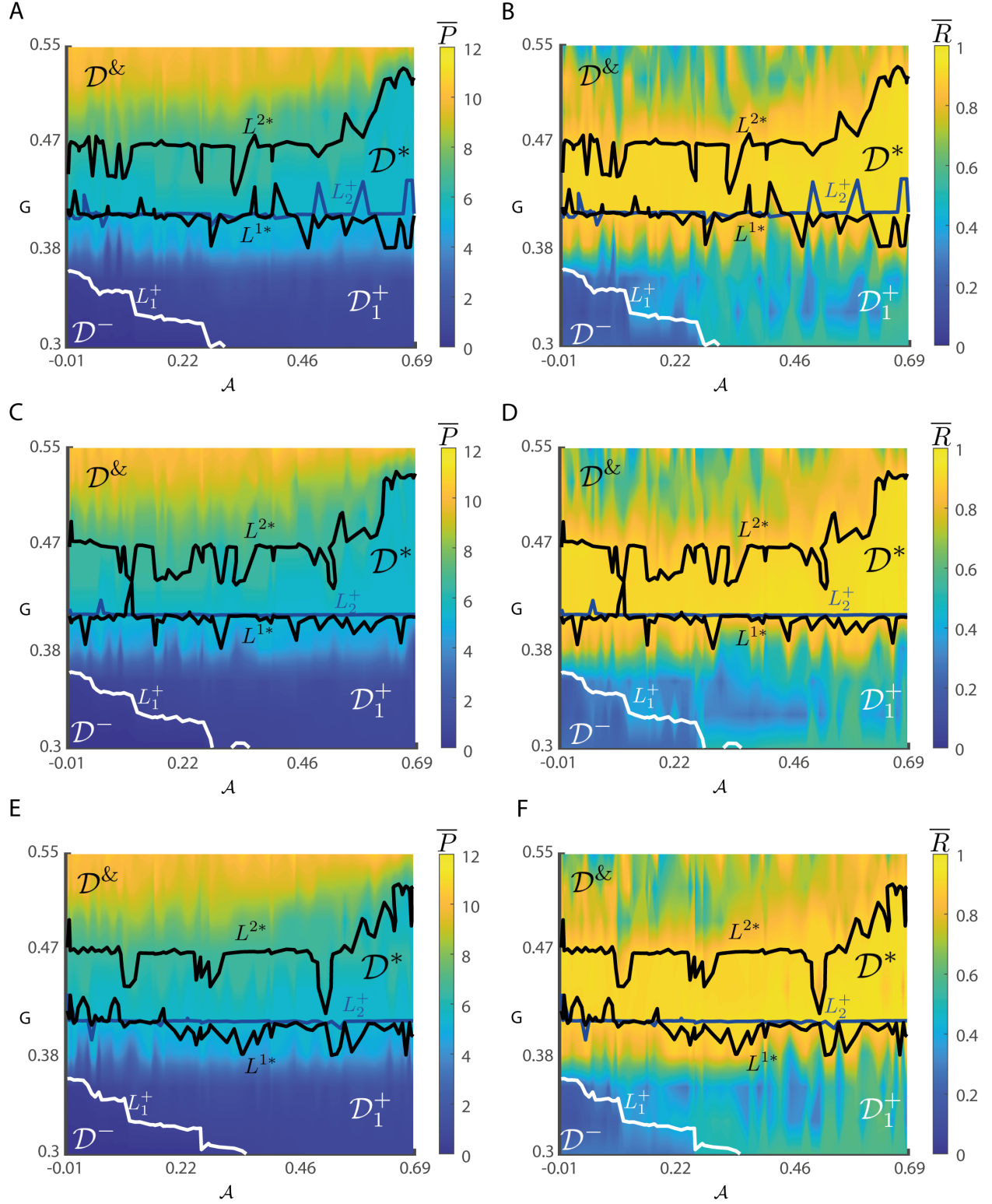


Figure S16. Network activity with respect to sortedness and drive for weak coupling (three initial conditions). A) \overline{P} for $Y_1(0)$. B) \overline{P} for $Y_1(0)$. C) \overline{P} for $Y_2(0)$. D) \overline{R} for $Y_2(0)$. E) \overline{P} for $Y_3(0)$. F) \overline{R} for $Y_3(0)$.

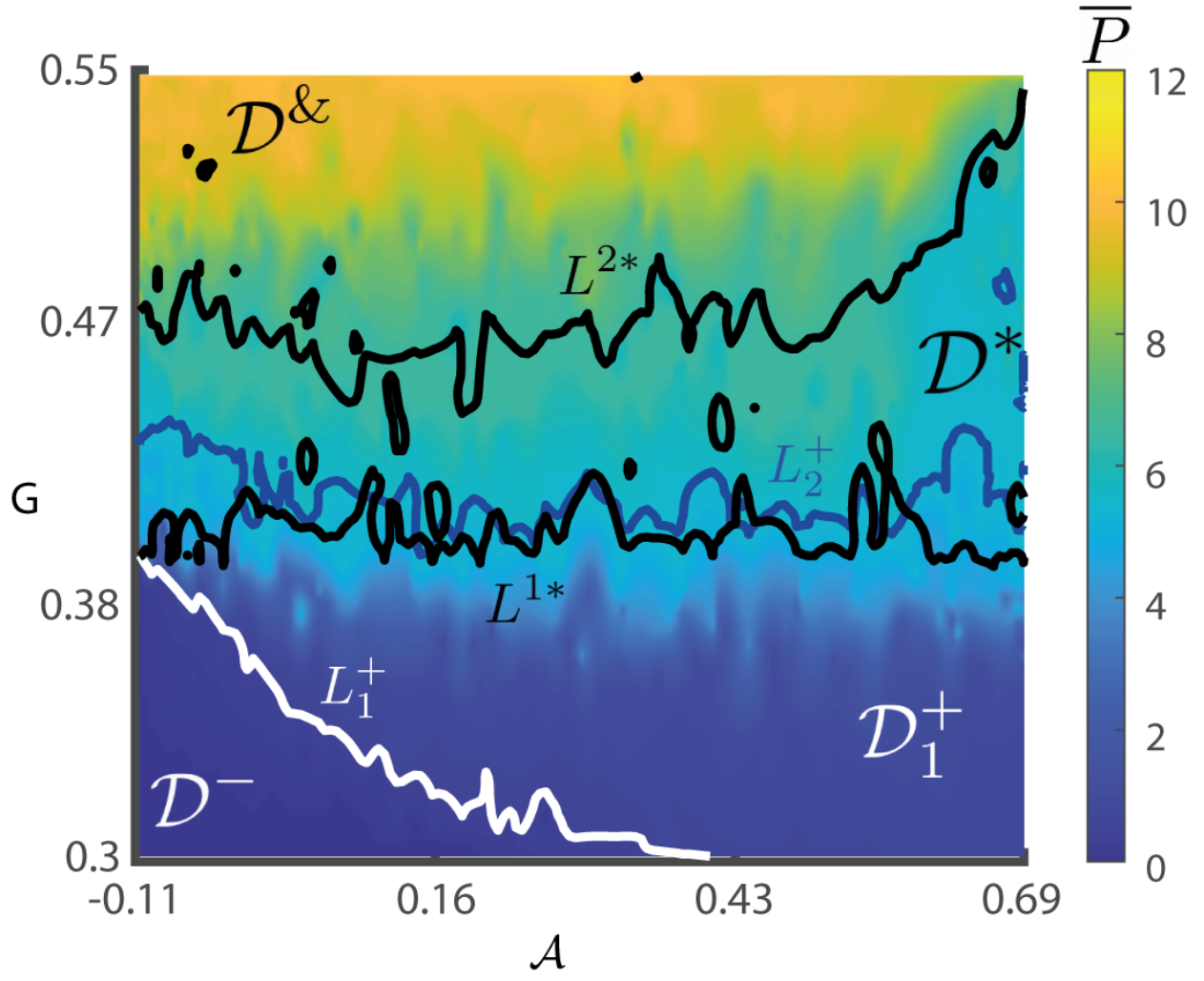


Figure S17. **Raw version of Fig. S7A.** This figure shows the complete level sets. We only kept the portions of the level sets L_1^+ , L_2^+ , L_1^* , and L_2^* that had analogues in Fig. S15A.